

---

# TOTAL PREDICTED MHC-I EPITOPE LOAD IS INVERSELY ASSOCIATED WITH POPULATION MORTALITY FROM SARS-CoV-2

---

**Eric A. Wilson**  
School of Molecular Sciences  
Arizona State University

**Gabrielle Hirneise**  
School of Life Sciences  
Arizona State University

**Abhishek Singharoy\***  
School of Molecular Sciences  
Arizona State University

**Karen S. Anderson\***  
Biodesign Institute  
Arizona State University

December 15, 2020

## ABSTRACT

Polymorphisms in MHC-I protein sequences across human populations significantly impacts viral peptide binding capacity and thus alters T cell immunity to infection. Consequently, allelic variants of the MHC-I protein have been found to be associated with patient outcome to various viral infections, including SARS-CoV. In the present study, we assess the relationship between observed SARS-CoV-2 population mortality and the predicted viral binding capacities of 52 common MHC-I alleles. Potential SARS-CoV-2 MHC-I peptides were identified using a consensus MHC-I binding and presentation prediction algorithm, called EnsembleMHC. Starting with nearly 3.5 million candidates, we resolved a few hundred highly probable MHC-I peptides. By weighing individual MHC allele-specific SARS-CoV-2 binding capacity with population frequency in 23 countries, we discover a strong inverse correlation between the predicted population SARS-CoV-2 peptide binding capacity and observed mortality rate. Our computations reveal that peptides derived from the structural proteins of the virus produces a stronger association with observed mortality rate, highlighting the importance of S, N, M, E proteins in driving productive immune responses. The correlation between epitope binding capacity and population mortality risk remains robust across a range of socioeconomic and epidemiological factors. A combination of binding capacity, number of deaths due to COPD complications, gender demographics, and the proportions of the population that were over the age of 65 and overweight offered the strongest determinant of at-risk populations. These results bring to light how molecular changes in the MHC-I proteins may affect population-level outcomes of viral infection.

**Keywords** SARS-CoV-2 · EnsembleMHC · MHC-I · risk-model · binding predictions · consensus models · population dynamics

---

\*corresponding author

## 0 Introduction

1 In December 2019, the novel coronavirus, SARS-CoV-2 was  
2 identified from a cluster of cases of pneumonia in Wuhan,  
3 China<sup>1,2</sup>. With over 73.1 million cases and over 1.6 million  
4 deaths, the viral spread has been declared a global pandemic by  
5 the World Health Organization<sup>3</sup>. Due to its high rate of trans-  
6 mission and unpredictable severity, there is an immediate need  
7 for information surrounding the adaptive immune response  
8 towards SARS-CoV-2.

9 A robust T cell response is integral for the clearance of  
10 coronaviruses, and generation of lasting immunity<sup>4</sup>. The poten-  
11 tial role of T cells for coronavirus clearance has been supported  
12 by the identification of immunogenic CD8<sup>+</sup> T cell epitopes in  
13 the S (Spike), N (Nucleocapsid), M (Membrane), and E (En-  
14 velope) proteins<sup>5</sup>. Additionally, SARS-CoV specific CD8<sup>+</sup> T  
15 cells have been shown to provide long lasting immunity with  
16 memory CD8<sup>+</sup> T cells being detected up to 17 years post infec-  
17 tion<sup>4,6,7</sup>. The specifics of the T cell response to SARS-CoV-  
18 2 peptides revealed a majority of the CD8<sup>+</sup> T cell immune  
19 response is targeted towards viral structural proteins (N, M,  
20 S)<sup>8</sup>.

22 A successful CD8<sup>+</sup> T cell response is contingent on the  
23 efficient presentation of viral protein fragments by Major Histo-  
24 compatibility Complex I (MHC-I) proteins. MHC-I molecules  
25 bind and present peptides derived from endogenous proteins  
26 on the cell surface for CD8<sup>+</sup> T cell interrogation. The MHC-I  
27 protein is highly polymorphic, with amino acid substitutions  
28 within the peptide binding groove drastically altering the com-  
29 position of presented peptides. Consequently, the influence  
30 of MHC genotype to shape patient outcome has been well  
31 studied in the context of viral infections<sup>9</sup>. For coronaviruses,  
32 there have been several studies of MHC association with dis-  
33 ease susceptibility. A study of a Taiwanese and Hong Kong  
34 cohort of patients with SARS-CoV found that the MHC-I alle-  
35 les HLA-B\*07:03 and HLA-B\*46:01 were linked to increased  
36 susceptibility while HLA-Cw\*15:02 was linked to increased  
37 resistance<sup>10-12</sup>. However, some of the reported associations  
38 did not remain after statistical correction, and it is still un-  
39 clear if MHC-outcome associations reported for SARS-CoV  
40 are applicable to SARS-CoV-2<sup>13,14</sup>. Recently, a comprehensive  
41 prediction of SARS-CoV-2 MHC-I peptides indicated a relative  
42 depletion of high affinity binding peptides for HLA-B\*46:01,  
43 hinting at a similar association profile in SARS-CoV-2<sup>15</sup>. More  
44 importantly, it remains elusive if such a depletion of putative  
45 high affinity peptides will impact patient outcome to SARS-  
46 CoV-2 infections.

47 The lack of large scale genomic data linking individual  
48 MHC genotype and outcome from SARS-CoV-2 infections

precludes a similar analysis as performed for SARS-CoV<sup>10-12</sup>.  
Therefore, we endeavored to assess the relationship between  
the predicted SARS-CoV-2 binding capacity of a population  
and the observed SARS-CoV-2 mortality rate. However, cur-  
rent MHC-I prediction algorithms have been characterized by  
a high false positive rate particularly when predicting peptides  
that are naturally presented<sup>16,17</sup>. To mitigate false positives and  
identify the highest confidence SARS-CoV-2 MHC-I peptides,  
we developed a consensus prediction algorithm, coined En-  
sembleMHC, and predicted MHC-I peptides for a panel of 52  
common MHC-I alleles<sup>18</sup>. This prediction workflow integrates  
seven different algorithms that have been parameterized on  
high-quality mass spectrometry data and provides a confidence  
level for each identified peptide<sup>17,19-24</sup>. The distribution of the  
number of high-confidence peptides assigned to each allele was  
used to assess a country-specific SARS-CoV-2 binding capacity,  
called the EnsembleMHC population score, for 23 countries  
(for selection criteria, please refer to the methods). This score  
was derived by weighing the individual binding capacities of  
the 52 MHC-I alleles by their endemic frequencies. We observe  
a strong inverse correlation between the EnsembleMHC popu-  
lation score and observed population SARS-CoV-2 mortality.  
Furthermore, the correlation is shown to become stronger when  
considering EnsembleMHC population scores based solely on  
SARS-CoV-2 structural proteins, underlining their potential im-  
portance in driving a robust immune response. Based on their  
predicted binding affinity, expression, and sequence conserva-  
tion in viral isolates, we identified 108 peptides derived from  
SARS-CoV-2 structural proteins that are high-value targets for  
CD8<sup>+</sup> T cell vaccine development.

## Results

**EnsembleMHC workflow offers more precise MHC-I pre-  
sentation predictions than individual algorithms.** The ac-  
curate assessment of differences in SARS-CoV-2 binding ca-  
pacities across MHC-I allelic variants requires the isolation  
of MHC-I peptides with a high probability of being presented.  
EnsembleMHC provides the requisite precision through the use  
of allele and algorithm-specific score thresholds and peptide  
confidence assignment.

MHC-I alleles substantially vary in both peptide bind-  
ing repertoire size and median binding affinity<sup>25</sup>. The Ensem-  
bleMHC workflow addresses this inter-allele variation by iden-  
tifying peptides based on MHC allele and algorithm-specific  
binding affinity thresholds. These thresholds were set by bench-  
marking each of the seven component algorithms against 52  
single MHC allele peptide data sets<sup>17</sup>. Each data set consists of  
mass spectrometry-confirmed MHC-I peptides that have been  
naturally presented by a model cell line expressing one of the 52

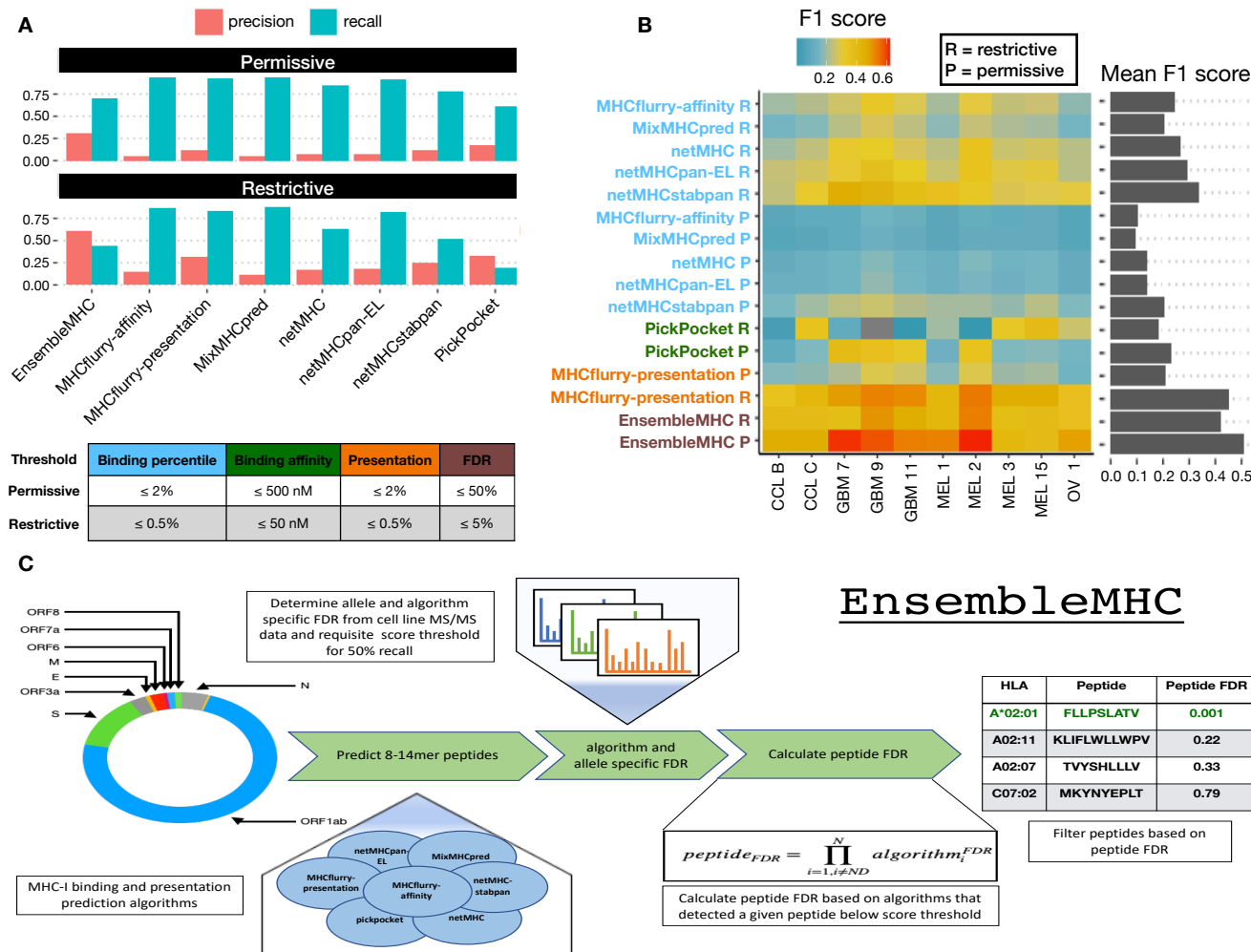


**Figure 1: Application of the EnsembleMHC prediction algorithm.** The EnsembleMHC prediction algorithm was used to recover MHC-I peptides from 10 tumor sample data sets. **A**, The average precision and recall for EnsembleMHC and each component algorithm was calculated across all 10 tumor samples. Peptide identification by each algorithm was based on commonly used restrictive (strong) or permissive (strong and weak) binding affinity thresholds (**inset table**). **B**, The F1 score of each algorithm was calculated for all tumor samples. Each algorithm is grouped into 1 of 4 categories: binding affinity represented by percentile score (blue), binding affinity represented by predicted peptide IC50 value (green), MHC-I presentation prediction (orange), and EnsembleMHC (brown). The heatmap colors indicate the value of the observed F1 score (color bar) for a given algorithm (y-axis) on a particular data set (x-axis). Warmer colors indicate higher F1 scores, and cooler colors indicate lower F1 scores. The average F1 score for each algorithm across all samples is shown in the marginal bar plot. **C**, The schematic for the application of the EnsembleMHC prediction algorithm to identify SARS-CoV-2 MHC-I peptides.

97 select MHC-I alleles. These experimentally validated peptides, 98 denoted target peptides, were supplemented with a 100-fold 99 excess of decoy peptides. Decoys were generated by randomly 100 sampling peptides that were not detected by mass spectrometry, 101 but were derived from the same protein sources as a detected 102 target peptide. Algorithm and allele-specific binding affinity 103 thresholds were then identified through the independent appli- 104 cation of each component algorithm to all MHC allele data sets.

For every data set and algorithm combination, the target and 105 decoy peptides were ranked by predicted binding affinity to 106 the MHC allele defined by that data set. Then, an algorithm- 107 specific binding affinity threshold was set to the minimum score 108 needed to isolate the highest affinity peptides commensurate 109 to 50% of the observed allele repertoire size (**methods, SI** 110 **A.1**). The observed allele repertoire size was defined as the 111 total number of target peptides within a given single MHC al- 112

113 lele data set. Therefore, if a data set had 1000 target peptides, 114 the top 500 highest affinity peptides would be selected, and 115 the algorithm-specific threshold would be set to the predicted 116 binding affinity of the 500<sup>th</sup> peptide. This parameterization 117 method resulted in the generation of a customized set of allele 118 and algorithm-specific binding affinity thresholds in which an 119 expected quantity of peptides can be recovered.

120 Consensus MHC-I prediction typically require a method 121 for combining outputs from each individual component algo- 122 rithm into a composite score. This composite score is then 123 used for peptide selection. EnsembleMHC identifies high- 124 confidence peptides based on filtering by a quantity called 125  $peptide^{FDR}$  (methods Eq. 1). During the identification of 126 allele and algorithm-specific binding affinity thresholds, the 127 empirical false detection rate (FDR) of each algorithm was cal- 128 culated. This calculation was based on the proportion of target 129 to decoy peptides isolated by the algorithm specific binding 130 affinity threshold. A  $peptide^{FDR}$  is then assigned to each indi- 131 vidual peptide by taking the product of the empirical FDRs of 132 each algorithm that identified that peptide for the same MHC-I 133 allele. Analysis of the parameterization process revealed that 134 the overall performance of each included algorithms was compar- 135 able, and there was diversity in individual peptide calls by 136 each algorithm, supporting an integrated approach to peptide 137 confidence assessment (SI A.2). Peptide identification by En- 138 sembleMHC was performed by selecting all peptides with a 139  $peptide^{FDR}$  of less than or equal to 5%<sup>26</sup>.

140 The efficacy of  $peptide^{FDR}$  as a filtering metric was de- 141 termined through the prediction of naturally presented MHC-I 142 peptides derived from ten tumor samples<sup>17</sup> (Figure 1). Similar 143 to the single MHC allele data sets, each tumor sample data set 144 consisted of mass spectrometry-detected target peptides and a 145 100-fold excess of decoy peptides. The relative performance of 146 EnsembleMHC was assessed via comparison with individual 147 component algorithms. Peptide identification by each algo- 148 rithm was based on a restrictive or permissive binding affinity 149 thresholds (Figure 1A (inset table)). For the component algo- 150 rithms, the permissive and restrictive thresholds correspond to 151 commonly used binding affinity cutoffs for the identification of 152 weak and strong binders, respectively<sup>27</sup>. The performance of 153 each algorithm on the ten data sets was evaluated through the 154 calculation of the empirical precision, recall, and F1 score.

155 The average precision and recall of each algorithm across 156 all tumor samples demonstrated an inverse relationship (Figure 157 1A). In general, restrictive binding affinity thresholds produced 158 higher precision at the cost of poorer recall. When comparing 159 the precision of each algorithm at restrictive thresholds, En- 160 sembleMHC demonstrated a 3.4-fold improvement over the 161 median precision of individual component algorithms. Ensem- 162 bleMHC also produced the highest F1 score with an average 163 of 0.51 followed by mhcfurry-presentation with an F1 score

164 of 0.45, both of which are 1.5-2 fold higher than the rest of 165 the algorithms (Figure 1B). result was shown to be robust 166 across a range of  $peptide^{FDR}$  cutoff thresholds (SI A.3) and 167 alternative performance metrics (SI A.4). Furthermore, Ensem- 168 bleMHC demonstrated the ability to more efficiently prioritize 169 peptides with experimentally established immunogenicity from 170 the Hepatitis-C genome polyprotein, the Dengue virus genome 171 polyprotein, and the HIV-1 POL-GAG protein (SI A.5). Taken 172 together, these results demonstrate the enhanced precision of 173 EnsembleMHC over individual component algorithms when 174 using common binding affinity thresholds.

175 In summary, the EnsembleMHC workflow offers two 176 desirable features. First, it determines allele-specific binding 177 affinity thresholds for each algorithm at which a known quantity 178 of peptides are expected to be successfully presented on the cell 179 surface. Second, it assigns a confidence level to each peptide 180 call made by each algorithm. Together, these traits enhance the 181 ability to identify MHC-I peptides with a high probability of 182 successful cell surface presentation.

183 EnsembleMHC was used to identify MHC-I peptides 184 for the SARS-CoV-2 virus (Figure 1C). The resulting identi- 185 fication of high-confidence SARS-CoV-2 peptides allows for 186 the characterization of alleles that are enriched or depleted 187 for predicted MHC-I peptides. The resulting distribution of 188 allele-specific SARS-CoV-2 binding capacities will then be 189 weighed by the normalized frequencies of the 52 alleles (SI A.6, 190 Methods Eq. 5-6) in 23 countries to determine the population- 191 specific SARS-CoV-2 binding capacity or EnsembleMHC pop- 192 ulation score (Methods Eq. 7). The potential impact of varying 193 population SARS-CoV-2 binding capacities on disease outcome 194 can then be assessed by correlating population SARS-CoV-2 195 mortality rates with EnsembleMHC population scores. Below, 196 we use EnsembleMHC population scores to stratify countries 197 based on their mortality risks.

198 **The MHC-I peptide-allele distribution for SARS-CoV-2** 199 **structural proteins is especially disproportionate.** MHC-I 200 peptides derived from the SARS-CoV-2 proteome were pre- 201 dicted and prioritized using EnsembleMHC. A total of 67,207 202 potential 8-14mer viral peptides were evaluated for each of the 203 considered MHC-I alleles. After filtering the pool of candi- 204 date peptides at the 5%  $peptide^{FDR}$  threshold, the number of 205 potential peptides was reduced from 3.49 Million to 971 (658 206 unique peptides) (SI A.7, SI table B.1). Illustrated in Figure 207 2A, the viral peptide-MHC allele (or peptide-allele) distribu- 208 tion for high-confidence SARS-CoV-2 peptides was determined 209 by assigning the identified peptides to their predicted MHC-I 210 alleles. There was a median of 16 peptides per allele with a 211 maximum of 47 peptides (HLA-A\*24:02), a minimum of 3 212 peptides (HLA-A\*02:05), and an interquartile range (IQR) of 213 16 peptides. Quality assurance of the predicted peptides was 214 performed by computing the peptide length frequencies and

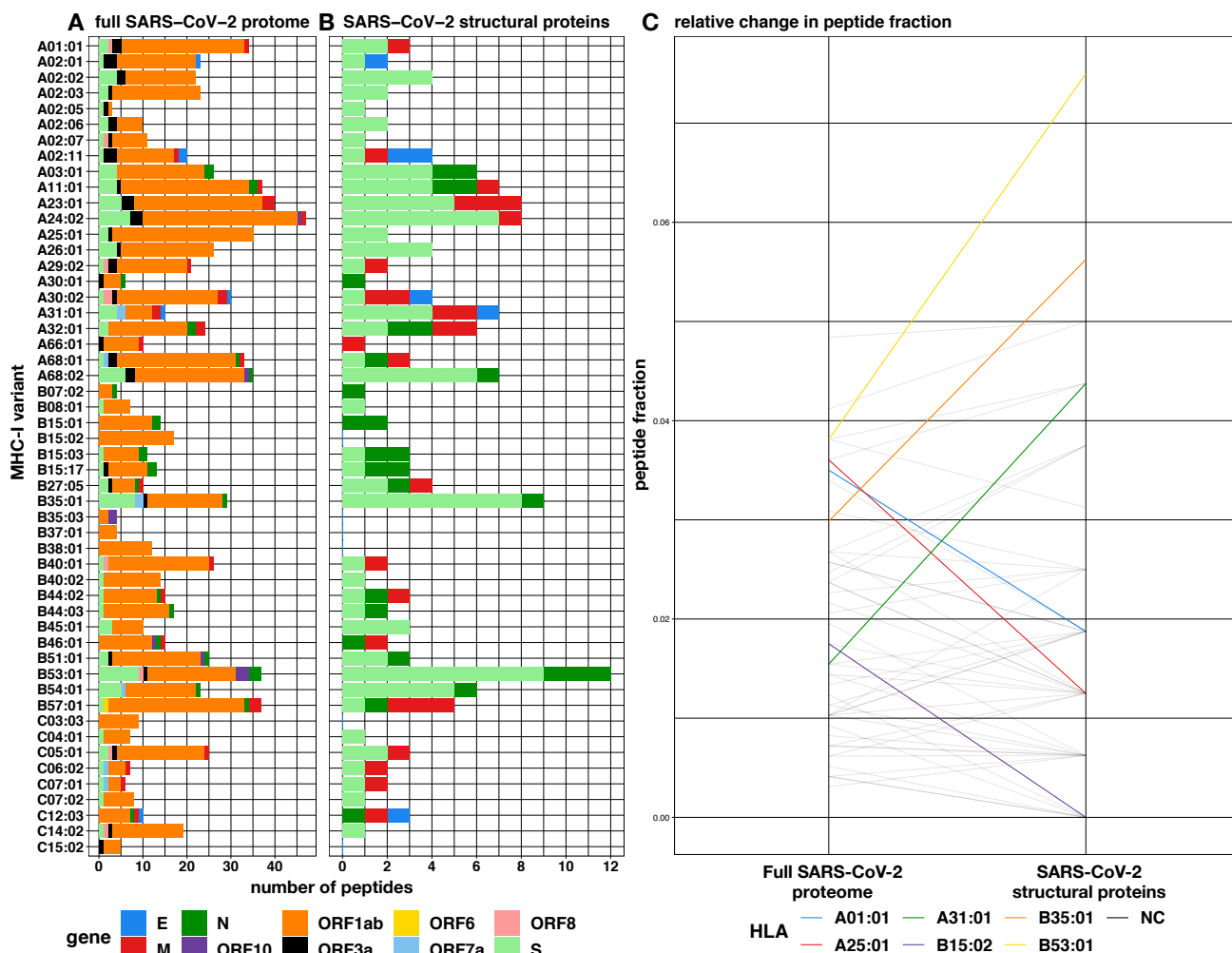


Figure 2: **Prediction of SARS-CoV-2 peptides across 52 common MHC-I alleles.** A-B, The EnsembleMHC workflow was used to predict MHC-I peptides for 52 alleles from the entire SARS-CoV-2 proteome or specifically SARS-CoV-2 structural proteins (envelope, spike, nucleocapsid, and membrane). C, The peptide fractions for both protein sets were calculated by dividing the number of peptides assigned to a given allele by the total number of identified peptides for that protein set. Each line indicates the change in peptide fraction observed by a given allele when comparing the viral peptide-MHC allele distribution for the full SARS-CoV-2 proteome or structural proteins. Alleles showing a change of greater than the median peptide fraction,  $\bar{X} = 0.015$ , are highlighted in color. For the performance of EnsembleMHC at a range of different  $peptide^{FDR}$  cutoff thresholds, refer to **SI A.3**

215 binding motifs. The predicted peptides were found to adhere to  
 216 expected MHC-I peptide lengths<sup>28</sup> with 78% of the peptides being  
 217 9 amino acids in length, 13% being 10 amino acids in length,  
 218 and 8% of peptides accounting for the remaining lengths (**SI**  
 219 **A.8**). Similarly, logo plots generated from predicted peptides  
 220 were found to closely reflect reference peptide binding motifs  
 221 for considered alleles<sup>29</sup> (**SI A.9**). Overall, the EnsembleMHC  
 222 prediction platform demonstrated the ability to isolate a short

list of potential peptides which adhere to expected MHC-I peptide characteristics.

The high expression, relative conservation, and reduced search space of SARS-CoV-2 structural proteins (S, E, M, and N) makes MHC-I binding peptides derived from these proteins high-value targets for CD8<sup>+</sup> T cell-based vaccine development. **Figure 2B** describes the peptide-allele distribution for predicted MHC-I peptides originating from the four structural proteins. This analysis markedly reduces the number of con-

232 sidered peptides from 658 to 108 (**SI table B.1**). The median  
233 number of predicted SARS-CoV-2 structural peptides assigned  
234 to each MHC-I allele was found to be 2 with a maximum of  
235 12 peptides (HLA-B\*53:01), a minimum of 0 (HLA-B\*15:02,  
236 B\*35:03,B\*38:01,C\*03:03,C\*15:02), and a IQR of 3 peptides.  
237 Analysis of the molecular source of the identified SARS-CoV-2  
238 structural protein peptides revealed that they originate from en-  
239 riched regions that are highly conserved (**SI A.10-A.11**). This  
240 indicates that such peptides would be good candidates for tar-  
241 geted therapies as they are unlikely to be disrupted by mutation,  
242 and several peptides can be targeted using minimal stretches  
243 of the source protein. Altogether, consideration of MHC-I  
244 peptides derived only from SARS-CoV-2 structural proteins  
245 reduces the number of potential peptides to a condensed set of  
246 high-value targets that is amenable to experimental validation.

247 Both the peptide-allele distributions, namely the ones de-  
248 rived from the full SARS-CoV-2 proteome and those from the  
249 structural proteins, were found to significantly deviate from an  
250 even distribution of predicted peptides as apparent in **figure**  
251 **2AB** and reflected in the Kolmogorov-Smirnov test p-values  
252 (**SI A.12**, full proteome =  $5.673e-07$  and structural proteins  
253 =  $1.45e-02$ ). These results support a potential allele-specific  
254 hierarchy for SARS-CoV-2 peptide presentation.

255 To determine if the MHC-I binding capacity hierarchy  
256 was consistent between the full SARS-CoV-2 proteome and  
257 SARS-CoV-2 structural proteins, the relative changes in the ob-  
258 served peptide fraction (number of peptides assigned to an allele  
259 / total number of peptides) between the two protein sets was vi-  
260 sualized (**Figure 2C**). Six alleles demonstrated changes greater  
261 than the median peptide fraction ( $\bar{X} = 0.015$ ) when comparing  
262 the two protein sets. The greatest decrease in peptide fraction  
263 was observed for A\*25:01 (1.52 times the median peptide frac-  
264 tion), and the greatest increase was seen with B\*53:01 (2.38  
265 times the median peptide fraction). Furthermore, the resulting  
266 SARS-CoV-2 structural protein peptide-allele distribution was  
267 found to be more variable than the distribution derived from the  
268 full SARS-CoV-2 proteome with a quartile coefficient of disper-  
269 sion of 0.6 compared to 0.44, respectively. This indicates that  
270 peptides derived from SARS-CoV-2 structural proteins experi-  
271 ence larger relative inter-allele binding capacity discrepancies  
272 than peptides derived from the the full SARS-CoV-2 proteome.  
273 Together, these results indicate a potential MHC-I binding ca-  
274 pacity hierarchy that is more pronounced for SARS-CoV-2  
275 structural proteins.

276 **Total population epitope load inversely correlates with re-**  
277 **ported death rates from SARS-CoV-2.** The documented im-  
278 portance of MHC-I peptides derived from SARS-CoV-2 struc-  
279 tural proteins<sup>8</sup>, coupled with the observed MHC allele bind-  
280 ing capacity hierarchy and the high immunogenicity rate of  
281 SARS-CoV-2 structural protein MHC-I peptides identified by  
282 EnsembleMHC (95% peptides tested *in vitro*, SI A.13), prompts

283 a potential relationship between MHC-I genotype and infec-  
284 tion outcome. However, due to the absence of MHC genotype  
285 data for SARS-CoV-2 patients, we assessed this relationship at  
286 the population-level by correlating predicted country-specific  
287 SARS-CoV-2 binding capacity (or EnsembleMHC population  
288 score) with observed SARS-CoV-2 mortality.

289 EnsembleMHC population scores (EMP) were deter-  
290 mined for 23 countries (**SI B.2**) by weighing the individual  
291 binding capacities of 52 common MHC-I alleles by their nor-  
292 malized endemic expression<sup>18</sup> (**methods, SI A.6**). This results  
293 in every country being assigned two separate EMP scores, one  
294 calculated with respect to the 108 unique SARS-CoV-2 struc-  
295 tural protein peptides (structural protein EMP) and the other  
296 with respect to the 658 unique peptides derived from the full  
297 SARS-CoV-2 proteome (full proteome EMP). The EMP score  
298 corresponds to the average predicted SARS-CoV-2 binding ca-  
299 pacity of a population. Therefore, individuals in a country with  
300 a high EMP score would be expected, on average, to present  
301 more SARS-CoV-2 peptides to CD8<sup>+</sup> T cells than individuals  
302 from a country with a low EMP score. The resulting EMP  
303 scores were then correlated with observed SARS-CoV-2 mor-  
304 tality (deaths per million) as a function of time. Temporal  
305 variance in community spread within the cohort of countries  
306 was corrected by truncating the SARS-CoV-2 mortality data  
307 set for each country to start after a certain minimum death  
308 threshold was met. For example, if the minimum death thresh-  
309 old was 50, then day 0 would be when each country reported  
310 at least 50 deaths. The number of countries included in each  
311 correlation decreases as the number of days increases due to  
312 discrepancies in the length of time that each country met a given  
313 minimum death threshold (**SI table B.3**). Therefore, the cor-  
314 relation between EMP score and SARS-CoV-2 mortality was  
315 only estimated at time points where there were at least eight  
316 countries. The eight country threshold was chosen because it is  
317 the minimum sample size needed to maintain sufficient power  
318 when detecting large effect sizes ( $\rho > 0.85$ ). The strength of the  
319 relationship between EMP score and SARS-CoV-2 mortality  
320 was determined using Spearman's rank-order correlation (for  
321 details concerning the choice of statistical tests, please refer  
322 to the methods section). Accordingly, both EMP scores and  
323 SARS-CoV-2 mortality data were converted into ascending  
324 ranks with the lowest rank indicating the minimum value and  
325 the highest rank indicating the maximum value. For instance, a  
326 country with an EMP score rank of 1 and death per million rank  
327 of 23 would have the lowest predicted SARS-CoV-2 binding  
328 capacity and the highest level of SARS-CoV-2-related mortal-  
329 ity. Using the described paradigm, the structural protein EMP  
330 score and the full proteome EMP score were correlated with  
331 SARS-CoV-2-related deaths per million for 23 countries.

332 Total predicted population SARS-CoV-2 binding capacity  
333 exhibited a strong inverse correlation with observed deaths per

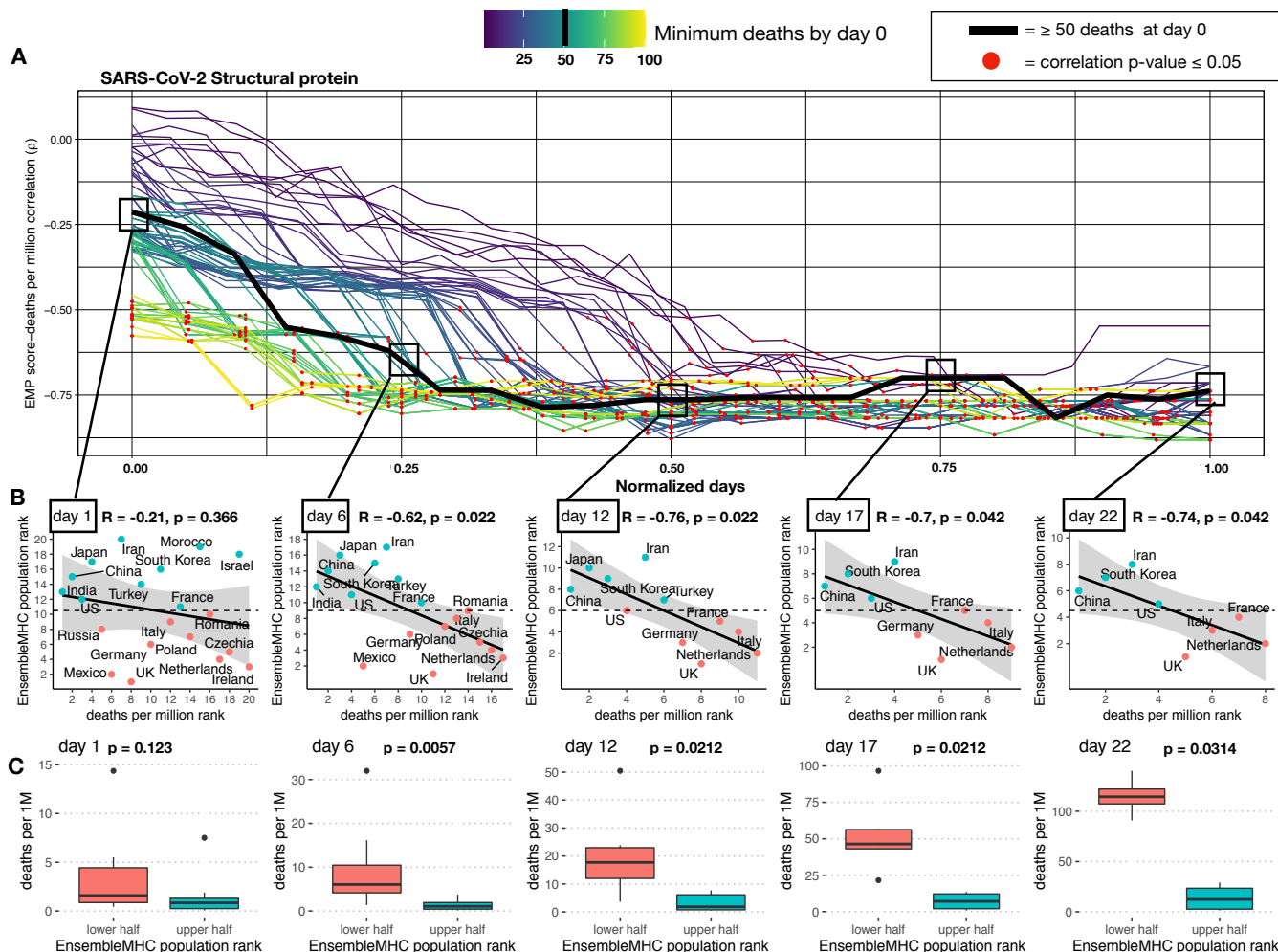


**Figure 3: Predicted total epitope load within a population inversely correlates with mortality.** **A**, SARS-CoV-2 structural protein-based EnsembleMHC population scores were assigned to 23 countries (SI B.2), and correlated with observed mortality rate (deaths per million). The correlation coefficient is presented as a function of time. Individual country mortality rate data were aligned by truncating each data set to start after a minimum threshold of deaths was observed in a given country (line color). The Spearman's rank correlation coefficient between structural protein EMP score and SARS-CoV-2 mortality rate was calculated at every day following day 0 for each of the minimum death thresholds. Due to the differing lengths of time series analysis at each minimum death threshold, the number of days were normalized to improve visualization. Thus, normalized day 0 represents the day when qualifying countries recorded at least the number of deaths indicated by the minimum death threshold, and normalized day 1 represents the final time point at which a correlation was measured. (For mapping between real and normalized days, see SI B.2). Correlations that were shown to be statistically significant ( $p$ -value  $\leq 0.05$ ) are indicated by a red point. **B**, The correlations between the structural protein EnsembleMHC population score (y-axis) and deaths per million (x-axis) were shown for countries meeting the 50 minimum deaths threshold at days 1, 6, 12, 17, and 22. Correlation coefficients and p-values were assigned using Spearman's rank correlation and the shaded region signifies the 95% confidence interval. Due to Spearman's rank correlation only considering data rank, Deaths per million and EnsembleMHC population score were converted to ascending rank values (low rank = low values, high rank = high values) to improve visualization of the measured relationship. Red points indicate a country that has an EnsembleMHC population rank less than the median EnsembleMHC population rank of all countries at that day, and blue points indicate a country with an EnsembleMHC population rank greater than the median EnsembleMHC population rank. **C**, The countries at each day were partitioned into a upper or lower half based on the median observed EnsembleMHC population rank. Therefore, countries with an EnsembleMHC population rank greater than the median group EnsembleMHC population score were assigned to the upper half (red), and the remaining countries were assigned to the lower half (blue). p-values were determined by Mann-Whitney U test. The presented box plots are in the style of Tukey (box defined by 25%, 50%, 75% quantiles, and whiskers  $\pm 1.5 \times$  IQR). The increasing gap between the red and the blue box plots indicates a greater discrepancy in the number of deaths per million between the two groups. The p values in all figures were corrected using the Benjamini-Hochberg procedure<sup>30</sup> relative to the number of tests performed for each death threshold

334 million. This relationship was found to be true for correlations  
335 based on the structural protein EMP (**Figure 3A**) and full proteome  
336 EMP (**SI A.14**) scores with a mean effect size of -0.66  
337 and -0.60, respectively. Significance testing of the correlations  
338 produced by both EMP scores revealed that the majority of  
339 reported correlations are statistically significant with 63% at-  
340 taining a p-value of  $\leq 0.05$ . Correlations based on the structural  
341 protein EMP score demonstrated a 24% higher proportion of  
342 statistically significant correlations compared to the full proteome  
343 EMP score (74% vs 51%). Furthermore, correlations  
344 for EMP scores based on structural proteins produced narrower  
345 95% confidence intervals (**SI A.15-A.16**, **SI table B.3**). Due  
346 to relatively low statistical power of the obtained correlations  
347 (**SI A.17**), the positive predictive value for each correlation  
348 (**methods, Eq. 8**) was calculated. The resulting proportions  
349 of correlations with a positive predictive value of  $\geq 95\%$  were  
350 similar to the observed significant p-value proportions with  
351 62% of all measured correlations, 72% of structural protein  
352 EMP score correlations, and 52% full proteome EMP score  
353 correlations (**SI A.14**). The similar proportions of significant  
354 p-values and PPVs supports that an overall true association is  
355 being captured. Furthermore, analysis of similar sized peptide  
356 sets sampled from the full SARS-CoV-2 proteome revealed that  
357 the observed distinction between the correlations produced by  
358 the two protein groups are unlikely to be due to differences in  
359 peptide set sizes (**SI A.18**).

360 Finally, the reported correlations did not remain after ran-  
361 domizing the allele assignment of predicted peptides prior to  
362 *peptide*<sup>FDR</sup> filtering (**SI A.19**), through the use of any indi-  
363 vidual algorithm (**SI A.20**). This indicates that the observed  
364 relationship is contingent on the high-confidence peptide-allele  
365 distribution produced by the EnsembleMHC prediction algo-  
366 rithm. Altogether, these data demonstrate that the MHC-I allele  
367 hierarchy characterized by EnsembleMHC is inversely asso-  
368 ciated with SARS-CoV-2 population mortality, and that the  
369 relationship becomes stronger when considering only the pre-  
370 sentation of SARS-CoV-2 structural proteins.

371 The ability to use structural protein EMP score to identify  
372 high and low risk populations was assessed using the median  
373 minimum death threshold (50 deaths) at evenly spaced time  
374 points (**Figure 3A, squares**). All correlations, with the excep-  
375 tion of day 1, were found to be significant with an average  
376 effect size of -0.71 (**Figure 3B**). Next, the countries at each  
377 day were partitioned into a high or low group based based on  
378 whether their assigned EMP score was higher or lower than  
379 the median observed EMP score (**Figure 3C**). The resulting  
380 grouping demonstrated a statistically significant difference in  
381 the median deaths per million between countries with low struc-  
382 tural protein EMP score and countries with high structural  
383 protein EMP scores. Additionally, it was observed that deaths  
384 per million increased much more rapidly in countries with low

385 structural protein EMP scores. Taken together, these results  
386 indicate that structural protein EMP score may be useful for  
387 assessing population risk from SARS-CoV-2 infections.

388 In summary, we make several important observations.  
389 First, there is a strong inverse correlation between predicted  
390 population SARS-CoV-2 binding capacity and observed deaths  
391 per million. This finding suggests that outcome to SARS-CoV-  
392 2 may be tied to total epitope load. Second, the correlation  
393 between predicted epitope load and population mortality is  
394 stronger for SARS-CoV-2 structural MHC-I peptides. This  
395 suggests that CD8<sup>+</sup> T cell-mediated immune response maybe  
396 primarily driven by recognition of epitopes derived from these  
397 proteins, a finding supported by recent T cell epitope mapping  
398 of SARS-CoV-2<sup>8</sup>. Finally, the EnsembleMHC population score  
399 can separate countries within the considered cohort into high  
400 or low risk populations.

#### 401 **Structural protein EMP score correlates better with popu-** 402 **lation outcome than identified individual risk factors.**

403 Recent large scale patient studies have identified several  
404 socioeconomic and health-related factors associated with in-  
405 creased risk of death from SARS-CoV-2 infections<sup>31,32</sup>. To  
406 delineate the relative importance of the structural protein EMP  
407 score as a SARS-CoV-2 severity descriptor, 12 additional risk  
408 factors were assessed for their ability to model population level  
409 SARS-CoV-2 outcome in 21 countries (**SI B.4**).

410 Overall, the structural protein EMP scores produced a  
411 significantly stronger association with population SARS-CoV-2  
412 mortality compared to other 12 descriptors (**Figure 4A**). While  
413 various effect size trends were observed, all additional covari-  
414 ates failed to produce statistically significant correlations. To  
415 determine if the modeling of SARS-CoV-2 mortality rate could  
416 be improved by the combination of single socioeconomic or  
417 health-related risk factors with structural protein EMP scores,  
418 a set of linear models consisting of either a single risk factor  
419 (single feature model) or that factor combined with structural  
420 protein EMP scores (combination model) were generated for  
421 every time point across each minimum death threshold (**meth-**  
422 **ods**). Following model generation, the adjusted coefficient of  
423 determination ( $R^2$ ) and significance level of each individual  
424 model was extracted and aggregated by dependent variable  
425 (**SI A.21**). Single feature models were characterized by low  
426  $R^2$  ( $\tilde{x} = -0.0262$ ) while combination models showed signifi-  
427 cant improvement ( $\tilde{x} = .496$ ). Similarly, combination models  
428 demonstrated a substantially higher proportion of statistical  
429 significance (**SI A.21B**). To determine the set of features that  
430 produce the best fitting model, all possible combinations of  
431 explanatory factors (risk factors and structural protein EMP  
432 score) were tested. Subsequently, the top ten performing mod-  
433 els, ranked by adjusted  $R^2$  value, were selected for analysis  
434 (**Figure 4B**). The identified models were found to be largely sig-



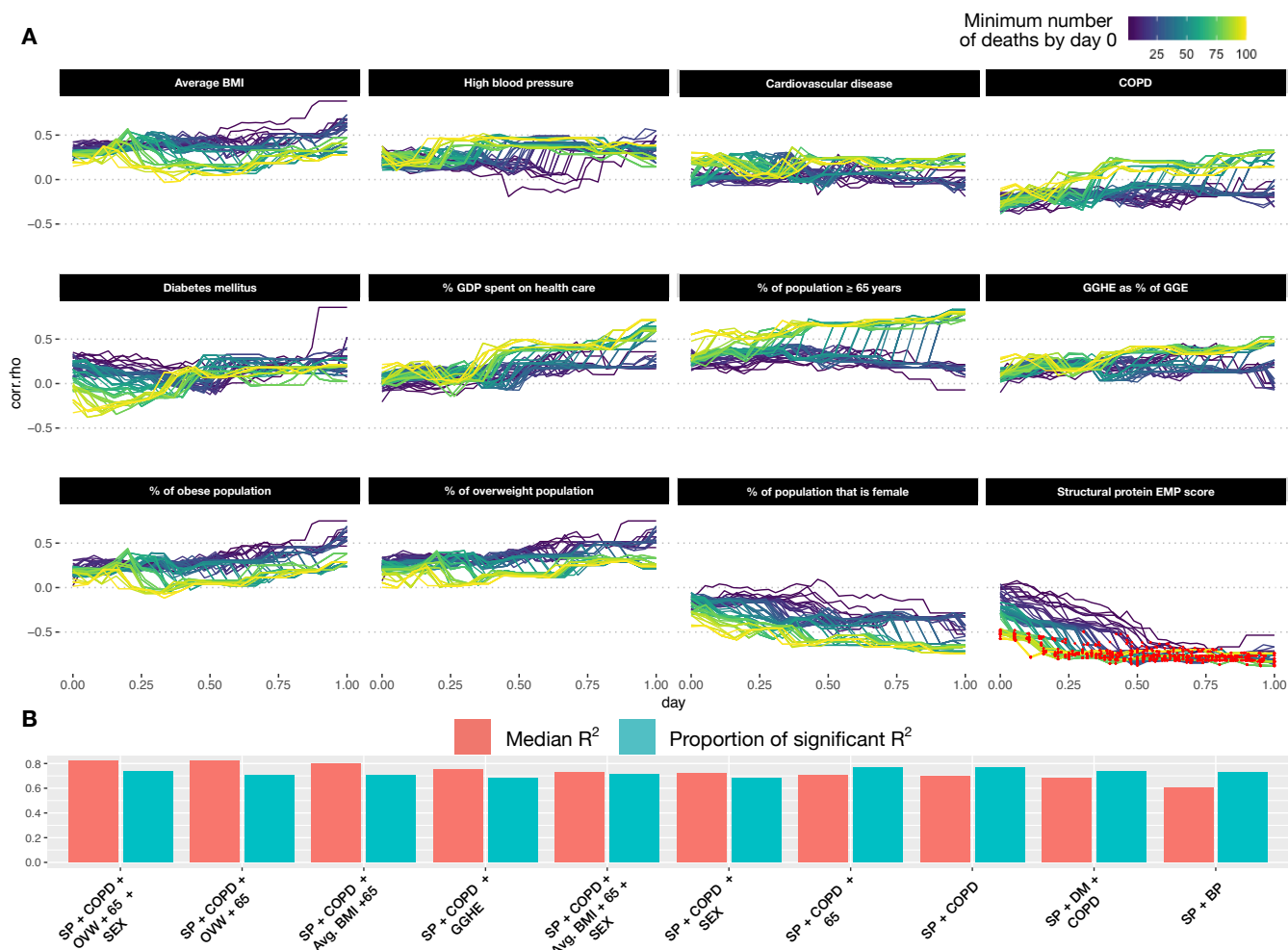


**Figure 4: Analysis of other SARS-CoV-2 covariates with observed SARS-CoV-2 population mortality and development of an integrative model.** **A**, 12 covariates associated with SARS-CoV-2 mortality on the individual patient level were assessed for correlation with population level mortality (SI table B.4). The correlation of each country-level covariate was determined at each time point after a minimum death threshold was met (line color). The x-axis represents the number of days (normalized) following when a minimum death threshold was met, and the y-axis indicates the observed effect size for that covariate at a given time point. Correlations achieving statistical significance are colored with a red dot. **B**, All possible combinations of covariates were used to fit a linear model. The top 10 models, ranked by median adjusted  $R^2$  (red bars), were identified (**B**). The proportion of regressions performed by that model that were found to be statistically significant (F-test 0.05) are represented by the blue bars.

435 nificant (average proportion of significant regressions = 72%)  
 436 and produce strong fits to the data (average  $R^2 = 0.7$ ).

437 Analysis of the dependent variables included in the top  
 438 performing models revealed that all models included structural  
 439 protein EMP scores followed by deaths per million due to  
 440 complications from COPD (90% of models). The median model  
 441 size included 3 features with a maximum of 5 features and a  
 442 minimum of 2 features. The model producing the best fit (me-

443 dian  $R^2 = 0.791$ ) consisted of structural protein EMP scores, 443  
 444 gender demographics, number of deaths due to COPD compli- 444  
 445 cations, the proportion of the population over the age of 65, 445  
 446 and proportion of the population that is overweight (**Figure 4B**). 446  
 447 All together, these results further indicate the robustness of the 447  
 448 structural protein EMP score as a population level risk descrip- 448  
 449 tor and identifies a potential candidate model for predicting 449  
 450 pandemic severity. 450

## 451 Discussion

452 In the present study, we uncover evidence supporting an associ- 501  
453 ation between population SARS-CoV-2 infection outcome and 502  
454 MHC-I genotype. In line with related work highlighting the 503  
455 relationship between total epitope load with HIV viral control<sup>33</sup>, 504  
456 we arrive at a working model that MHC-I alleles presenting 505  
457 more unique SARS-CoV-2 epitopes will be associated with 506  
458 lower mortality due to a higher number of potential T cell 507  
459 targets. The SARS-CoV-2 binding capacities of 52 common 508  
460 MHC-I alleles were assessed using the EnsembleMHC predic- 509  
461 tion platform. These predictions identified 971 high-confidence 510  
462 MHC-I peptides out of a candidate pool of nearly 3.5 million. In 511  
463 agreement with other *in silico* studies<sup>15,34</sup>, the assignment of the 512  
464 predicted peptides to their respective MHC-I alleles revealed an 513  
465 uneven distribution in the number of peptides attributed to each 514  
466 allele. We discovered that the MHC-I peptide-allele distribution 515  
467 originating from the full SARS-CoV-2 proteome undergoes a 516  
468 notable rearrangement when considering only peptides derived 517  
469 from viral structural proteins. The structural protein-specific 518  
470 peptide-allele distribution produced a distinct hierarchy of al- 519  
471 lele binding capacities. This finding has important clinical 520  
472 implications as a majority of SARS-CoV-2 specific CD8<sup>+</sup> T 521  
473 cell response is directed towards SARS-CoV-2 structural pro- 522  
474 teins<sup>8</sup>. Therefore, patients who express MHC-I alleles enriched 523  
475 with a large potential repertoire of SARS-CoV-2 structural pro- 524  
476 teins peptides may benefit from a broader CD8<sup>+</sup> T cell immune 525  
477 response. 526

478 The variations in SARS-CoV-2 peptide-allele distribu- 527  
479 tions were analyzed at epidemiological scale to track its impact 528  
480 on country-specific mortality. Each of the 23 countries were 529  
481 assigned a population SARS-CoV-2 binding capacity (or En- 530  
482 sembleMHC population score) based on the individual binding 531  
483 capacities of the selected 52 MHC-I alleles weighted by their 532  
484 endemic population frequencies. This hierarchization revealed 533  
485 a strong inverse correlation between EnsembleMHC population 534  
486 score and observed population mortality, indicating that popula- 535  
487 tions enriched with high SARS-CoV-2 binding capacity MHC-I 536  
488 alleles may be better protected. The correlation was shown to 537  
489 be stronger when calculating the EnsembleMHC population 538  
490 scores with respect to only structural proteins, reinforcing their 539  
491 relevance to viral immunity. Finally, The molecular origin of 540  
492 the 108 predicted peptides specific to SARS-CoV-2 structural 541  
493 proteins revealed that they are derived from enriched regions 542  
494 with a minimal predicted impact from amino acid sequence 543  
495 polymorphisms. 544

496 The utility of structural protein EnsembleMHC popula- 545  
497 tion scores was further supported by a multivariate analysis of 546  
498 additional SARS-CoV-2 risk factors. These results emphasized 547  
499 the relative robustness of structural protein EMP scores as a 548  
500 population risk assessment tool. Furthermore, a linear model 549

501 based on the combination of structural protein EMP scores and 502  
503 select population-level risk factors was identified a potential 504  
505 candidate for a predictive model for pandemic severity. As 506  
507 such, the incorporation of the structural protein EMP score in 508  
509 more sophisticated models will likely improve epidemiological 510  
511 modeling of pandemic severity. 512

513 In order to achieve the highest level of accuracy in MHC-I 514  
515 predictions, the most up-to-date versions of each component 516  
517 algorithm were used. However, this meant that several of the al- 518  
519 gorithms (MHCflurry, netMHCpan-EL-4.0 and MixMHCpred) 520  
521 were benchmarked against subsets of mass spectrometry data 522  
523 that were used in the original training of these MHC-I predic- 524  
525 tion models. While this could result in an unfair weight applied 526  
527 to these algorithms in *peptide*<sup>FDR</sup> calculation, the individual 528  
529 FDRs of MHCflurry, netMHCpan-EL-4.0 and MixMHCpred 530  
531 were comparable to algorithms without this advantage (**SI A.2**). 532  
533 Furthermore, the peptide selection of SARS-CoV-2 peptides 534  
535 was shown to be highly cooperative within EnsembleMHC (**SI** 536  
537 **A.7**), and individual algorithms failed to replicate the strong 538  
539 observed correlations between population binding capacity and 540  
541 observed SARS-CoV-2 mortality (**SI A.20**). 542

543 In the future, the presented model could be applied to pre- 544  
545 dict individual T cell capacity to mount a robust SARS-CoV-2 545  
546 immune response. Evolutionary divergence of patient MHC-I 546  
547 genotypes have shown to be predictive of response to immune 547  
548 checkpoint therapy in cancer and HIV<sup>35,36</sup>. However, confirma- 548  
549 tion will require large data sets associating individual patient 549  
550 MHC-I genotype and outcome. Additionally, future use of En- 551  
552 sembleMHC to design personalized T cell vaccines will require 552  
553 broad experimental validation of high scoring peptides, since 553  
554 EnsembleMHC predicts MHC-I peptides with a high proba- 554  
555 bility of antigen presentation as opposed to directly predicting 555  
556 peptide immunogenicity. While previous work has determined 556  
557 that a majority of successfully presented viral MHC-I peptides 557  
558 are immunogenic<sup>37</sup>, there is an expectation that some presented 558  
559 SARS-CoV-2 MHC-I peptides will fail to produce an immune 559  
560 response. 560

561 The current work assessed the relative importance of the 561  
562 structural protein EMP score with respect to other population- 562  
563 level risk factors (e.g. population incidence of risk-associated 563  
564 commodities, healthcare infrastructure, age, sex), however, it 564  
565 should be noted that the impacts these risk factors on patient 565  
566 outcome are likely to vary significantly on a individual basis. 566  
567 Furthermore, other genetic determinants of severity were not 567  
568 considered<sup>38</sup>. Therefore, a complete understanding of the rela- 568  
569 tive importance of MHC genotype and SARS-CoV-2 presenta- 569  
570 tion capacity on patient outcome will require the integration 570  
571 individual patient genetic and clinical data. 571

572 The versatility of the proposed model will be improved 572  
573 by the consideration of additional MHC-I alleles. To reduce 573

551 the presence of confounding factors, EnsembleMHC was pa- 595  
552 rameterized on only a subset of common MHC-I alleles that 596  
553 had strong existing experimental validation. While the selected 597  
554 MHC-I alleles are among some of the most common, person- 598  
555 alized risk assessment will require consideration of the full 599  
556 patient MHC-I genotype. The continued mass spectrometry- 600  
557 based characterization of MHC-I peptide binding motifs will 601  
558 help in this regard. However, due to the large potential se- 602  
559 quence space of the MHC-I protein, extension of this model 603  
560 will likely require inference of binding motifs based on MHC 604  
561 variant clustering. 605

## 562 Acknowledgments

563 We would like to thank Drs. Diego Chowell, Matthew Scotch, 606  
564 Sri Krishna, Shay Ferdosi, and Mr. John Vant, Mr. Ryan Boyd, 607  
565 and Ms. Mollie Peters for critical feedback and discussion. 608  
566 Finally, we would like to thank ASU Research computing for 609  
567 allocating the computational resources. 610

## 568 References

- 569 [1] Zi Yue Zu et al. “Coronavirus disease 2019 (COVID- 612  
570 19): a perspective from China”. In: *Radiology* (2020), 613  
571 p. 200490. 614
- 572 [2] Qun Li et al. “Early transmission dynamics in Wuhan, 615  
573 China, of novel coronavirus–infected pneumonia”. In: 616  
574 *New England Journal of Medicine* (2020). 617
- 575 [3] Yan-Rong Guo et al. “The origin, transmission and clinical 618  
576 therapies on coronavirus disease 2019 (COVID-19) 619  
577 outbreak—an update on the status”. In: *Military Medical 620  
578 Research* 7.1 (2020), pp. 1–10. 621
- 579 [4] Rudragouda Channappanavar, Jincun Zhao, and Stanley 622  
580 Perlman. “T cell-mediated immune response to respira- 623  
581 tory coronaviruses”. In: *Immunologic research* 59.1-3 624  
582 (2014), pp. 118–128. 625
- 583 [5] Hsueh-Ling Janice Oh et al. “Understanding the T cell 626  
584 immune response in SARS coronavirus infection”. In: 627  
585 *Emerging microbes & infections* 1.1 (2012), pp. 1–6. 628
- 586 [6] Oi-Wing Ng et al. “Memory T cell responses target- 629  
587 ing the SARS coronavirus persist up to 11 years post- 630  
588 infection”. In: *Vaccine* 34.17 (2016), pp. 2008–2014. 631
- 589 [7] Nina Le Bert et al. “SARS-CoV-2-specific T cell immu- 632  
590 nity in cases of COVID-19 and SARS, and uninfected 633  
591 controls”. In: *Nature* 584.7821 (2020), pp. 457–462. 634
- 592 [8] Alba Grifoni et al. “Targets of T cell responses to SARS- 635  
593 CoV-2 coronavirus in humans with COVID-19 disease 636  
594 and unexposed individuals”. In: *Cell* (2020). 637
- [9] Vasiliki Matzaraki et al. “The MHC locus and genetic 638  
susceptibility to autoimmune and infectious diseases”. 639  
In: *Genome biology* 18.1 (2017), p. 76. 640
- [10] Marie Lin et al. “Association of HLA class I with severe 641  
acute respiratory syndrome coronavirus infection”. In: 642  
*BMC Medical Genetics* 4.1 (2003), p. 9. 643
- [11] Sheng-Fan Wang et al. “Human-leukocyte antigen class 644  
I Cw 1502 and class II DR 0301 genotypes are associ-  
ated with resistance to severe acute respiratory syndrome  
(SARS) infection”. In: *Viral immunology* 24.5 (2011),  
pp. 421–426.
- [12] Margaret HL Ng et al. “Association of human-leukocyte-  
antigen class I (B\* 0703) and class II (DRB1\* 0301)  
genotypes with susceptibility and resistance to the de-  
velopment of severe acute respiratory syndrome”. In:  
*Journal of Infectious Diseases* 190.3 (2004), pp. 515–  
518.
- [13] MH Ng et al. “Immunogenetics in SARS: a case-control  
study.” In: *Hong Kong medical journal= Xianggang yi  
xue za zhi* 16.5 Suppl 4 (2010), p. 29.
- [14] Alicia Sanchez-Mazas. “HLA studies in the context  
of coronavirus outbreaks”. In: *Swiss Medical Weekly*  
150.1516 (2020).
- [15] Austin Nguyen et al. “Human leukocyte antigen suscep-  
tibility map for SARS-CoV-2”. In: *Journal of Virology*  
(2020).
- [16] Weilong Zhao and Xinwei Sher. “Systematically bench-  
marking peptide-MHC binding predictors: From syn-  
thetic to naturally processed epitopes”. In: *PLoS compu-  
tational biology* 14.11 (2018).
- [17] Siranush Sarkizova et al. “A large peptidome dataset  
improves HLA class I epitope prediction across most of  
the human population”. In: *Nature Biotechnology* 38.2  
(2020), pp. 199–209.
- [18] Faviel F González-Galarza et al. “Allele frequency net  
2015 update: new features for HLA epitopes, KIR and  
disease and HLA adverse drug reaction associations”. In:  
*Nucleic acids research* 43.D1 (2015), pp. D784–D788.
- [19] Timothy J O’Donnell, Alex Rubinsteyn, and Uri Laser-  
son. “MHCflurry 2.0: Improved Pan-Allele Prediction  
of MHC Class I-Presented Peptides by Incorporating  
Antigen Processing”. In: *Cell Systems* (2020).
- [20] Vanessa Jurtz et al. “NetMHCpan-4.0: improved peptide-  
MHC class I interaction predictions integrating eluted  
ligand and peptide binding affinity data”. In: *The Journal  
of Immunology* 199.9 (2017), pp. 3360–3368.
- [21] Massimo Andreatta and Morten Nielsen. “Gapped se-  
quence alignment using artificial neural networks: appli-  
cation to the MHC class I system”. In: *Bioinformatics*  
32.4 (2016), pp. 511–517.

- 645 [22] Michal Bassani-Sternberg et al. “Deciphering HLA-I 696  
646 motifs across HLA peptidomes improves neo-antigen 697  
647 predictions and identifies allosteric regulating HLA speci- 698  
648 ficity”. In: *PLoS computational biology* 13.8 (2017), 699  
649 e1005725. 700
- 650 [23] Hao Zhang, Ole Lund, and Morten Nielsen. “The Pick- 701  
651 Pocket method for predicting binding specificities for 702  
652 receptors based on receptor pocket similarities: applica- 703  
653 tion to MHC-peptide binding”. In: *Bioinformatics* 25.10 704  
654 (2009), pp. 1293–1299. 705
- 655 [24] Michael Rasmussen et al. “Pan-specific prediction of 706  
656 peptide–MHC class I complex stability, a correlate of T 707  
657 cell immunogenicity”. In: *The Journal of Immunology* 708  
658 197.4 (2016), pp. 1517–1524. 709
- 659 [25] Sinu Paul et al. “HLA class I alleles are associated 710  
660 with peptide-binding repertoires of different size, affinity, 711  
661 and immunogenicity”. In: *The Journal of Immunology* 712  
662 191.12 (2013), pp. 5831–5839. 713
- 663 [26] K Nichols. “False discovery rate procedures”. In: *Sta- 714  
664 tistical Parametric Mapping*. Elsevier, 2007, pp. 246– 715  
665 252. 716
- 666 [27] Morten Nielsen et al. “Immunoinformatics: Predicting 717  
667 Peptide–MHC Binding”. In: *Annual Review of Biomed- 718  
668 ical Data Science* 3 (2020). 719
- 669 [28] Thomas Trolle et al. “The length distribution of class I– 720  
670 restricted T cell epitopes is determined by both peptide 721  
671 supply and MHC allele–specific binding preference”. 722  
672 In: *The Journal of Immunology* 196.4 (2016), pp. 1480– 723  
673 1487. 724
- 674 [29] Nicolas Rapin et al. “The MHC motif viewer: a visualiza- 725  
675 tion tool for MHC binding motifs”. In: *Current protocols 726  
676 in immunology* 88.1 (2010), pp. 18–17. 727
- 677 [30] Yoav Benjamini and Yocef Hochberg. “Controlling the 728  
678 false discovery rate: a practical and powerful approach 729  
679 to multiple testing”. In: *Journal of the Royal statistical 730  
680 society: series B (Methodological)* 57.1 (1995), pp. 289– 731  
681 300. 732
- 682 [31] Elizabeth J Williamson et al. “OpenSAFELY: factors 733  
683 associated with COVID-19 death in 17 million patients”. 734  
684 In: *Nature* (2020), pp. 1–11. 735
- 685 [32] Simon de Lusignan et al. “Risk factors for SARS-CoV-2 736  
686 among patients in the Oxford Royal College of General 737  
687 Practitioners Research and Surveillance Centre primary 738  
688 care network: a cross-sectional study”. In: *The Lancet 739  
689 Infectious Diseases* (2020). 740
- 690 [33] Morgane Rolland et al. “Broad and Gag-biased HIV-1 741  
691 epitope repertoires are associated with lower viral loads”. 742  
692 In: *PloS one* 3.1 (2008). 743
- 693 [34] Katie M Campbell et al. “Prediction of SARS-CoV-2 744  
694 epitopes across 9360 HLA class I alleles”. In: *bioRxiv* 745  
695 (2020). 746
- 700 [35] Diego Chowell et al. “Evolutionary divergence of HLA 747  
701 class I genotype impacts efficacy of cancer immunother- 748  
702 apy”. In: *Nature medicine* 25.11 (2019), pp. 1715–1720. 749
- 703 [36] Jatin Arora et al. “HLA heterozygote advantage against 750  
704 HIV-1 is driven by quantitative and qualitative differ- 751  
705 ences in HLA allele-specific peptide presentation”. In: 752  
706 *Molecular biology and evolution* 37.3 (2020), pp. 639– 753  
707 650. 754
- 708 [37] Nathan P Croft et al. “Most viral peptides displayed by 755  
709 class I MHC on infected cells are immunogenic”. In: 756  
710 *Proceedings of the National Academy of Sciences* 116.8 757  
711 (2019), pp. 3112–3117. 758
- 712 [38] Yanan Cao et al. “Comparative genetic analysis of the 759  
713 novel coronavirus (2019-nCoV/SARS-CoV-2) receptor 760  
714 ACE2 in different populations”. In: *Cell discovery* 6.1 761  
715 (2020), pp. 1–4. 762
- 716 [39] Marek Prachar et al. “COVID-19 Vaccine Candidates: 763  
717 Prediction and Validation of 174 SARS-CoV-2 Epi- 764  
718 topes”. In: *bioRxiv* (2020). 765
- 719 [40] Syed Faraz Ahmed, Ahmed A Quadeer, and Matthew R 766  
720 McKay. “COVIDep: A web-based platform for real-time 767  
721 reporting of vaccine target recommendations for SARS- 768  
722 CoV-2”. In: *Nature reviews microbiology* 15 (2020), 769  
723 pp. 2141–2142. 770
- 724 [41] Helen M Berman et al. “The protein data bank”. In: *Nu- 771  
725 cleic acids research* 28.1 (2000), pp. 235–242. 772
- 726 [42] Chengxin Zhang et al. “Protein structure and sequence 773  
727 re-analysis of 2019-nCoV genome refutes snakes as its 774  
728 intermediate host or the unique similarity between its 775  
729 spike protein insertions and HIV-1”. In: *Journal of pro- 776  
730 teome research* (2020). 777
- 731 [43] William Humphrey, Andrew Dalke, Klaus Schulten, et 778  
732 al. “VMD: visual molecular dynamics”. In: *Journal of 779  
733 molecular graphics* 14.1 (1996), pp. 33–38. 780
- 734 [44] Ensheng Dong, Hongru Du, and Lauren Gardner. “An 781  
735 interactive web-based dashboard to track COVID-19 in 782  
736 real time”. In: *The Lancet infectious diseases* (2020). 783
- 737 [45] Katherine S Button et al. “Power failure: why small sam- 784  
738 ple size undermines the reliability of neuroscience”. In: 785  
739 *Nature Reviews Neuroscience* 14.5 (2013), pp. 365–376. 786
- 740 [46] Andrew P Ferretti et al. “COVID-19 patients form mem- 787  
741 ory CD8+ T cells that recognize a small set of shared 788  
742 immunodominant epitopes in SARS-CoV-2”. In: (2020). 789
- 743 [47] Annika Nelde et al. “SARS-CoV-2-derived peptides de- 790  
744 fine heterologous and COVID-19-induced T cell recog- 791  
745 nition”. In: *Nature immunology* (2020), pp. 1–12. 792
- 746 [48] Thomas M Snyder et al. “Magnitude and dynamics of 793  
747 the T-cell response to SARS-CoV-2 infection at both 794  
748 individual and population levels”. In: *medRxiv* (2020). 795

- 745 [49] Ahmed A Quadeer, Syed Faraz Ahmed, and Matthew R  
746 McKay. “Epitopes targeted by T cells in convalescent  
747 COVID-19 patients”. In: *bioRxiv* (2020).

## 748 Methods

### 749 EnsembleMHC prediction workflow

750 **EnsembleMHC component binding and processing predic-**  
751 **tion algorithms.** EnsembleMHC incorporates MHC-I binding  
752 and processing predictions from 7 publicly available algorithms:  
753 MHCflurry-affinity-1.6.0<sup>19</sup>, MHCflurry-presentation-1.6.0<sup>19</sup>,  
754 netMHC-4.0<sup>21</sup>, netMHCpan-4.0-EL<sup>20</sup>, netMHCstabpan-1.0<sup>24</sup>,  
755 PickPocket-1.1<sup>23</sup> and, MixMHCpred-2.0.2<sup>22</sup>. These algorithms  
756 were chosen based on the criteria of providing a free academic  
757 license, bash command line integration, and demonstrated ac-  
758 curacy for predicting SARS-CoV-2 MHC-I peptides with ex-  
759 perimentally validated binding stability<sup>39</sup>.

760 Each of the selected algorithms cover components of  
761 MHC-I binding and antigen processing that roughly fall into  
762 two categories: ones based primarily on MHC-I binding affini-  
763 ty predictions and others that model antigen presentation.  
764 To this end, MHCflurry-affinity, netMHC, PickPocket, and  
765 netMHCstabpan predict binding affinity based on quantitative  
766 peptide binding affinity measurements. netMHCstabpan also  
767 incorporates peptide-MHC stability measurements and Pick-  
768 Pocket performs prediction based on binding pocket structural  
769 extrapolation. To model the effects of antigen presentation,  
770 MixMHCpred, netMHCpan-EL, and MHCflurry-presentation  
771 are trained on naturally eluted MHC-I ligands. Additionally,  
772 MHCflurry-presentation incorporates an antigen processing  
773 term.

774 **Parameterization of EnsembleMHC using mass spectrom-**  
775 **etry data.** EnsembleMHC is able to achieve high levels of  
776 precision in peptide selection through the use of allele and  
777 algorithm-specific binding affinity thresholds. These binding  
778 affinity thresholds were identified through the parameterization  
779 of each algorithm on high-quality mass spectrometry data sets<sup>17</sup>.  
780 The mass spectrometry data sets used for algorithm parameteri-  
781 zation were collected in the largest single laboratory MS-based  
782 characterization of MHC-I peptides presented by single MHC  
783 allele cell lines. These characteristics significantly reduces the  
784 number of artifacts introduced by differences in peptide isola-  
785 tion methods, mass spectrometry acquisition, and convolution  
786 of peptides in multiallelic cell lines. An overview of the Ensem-  
787 bleMHC parameterization is provided in supplemental figures  
788 (SI A.1).

789 Fifty-two common MHC-I alleles were selected for pa-  
790 rameterization based on the criteria that they were characterized  
791 in *Sarkizova et al.* data sets and that all 7 component algorithms  
792 could perform peptide binding affinity predictions for that allele.  
793 Each target peptide (observed in the MS data set) was paired  
794 with 100 length-matched randomly sampled decoy peptides  
795 (not observed in the MS data set) derived from the same source

796 proteins. If a protein was less than 100 amino acids in length,  
797 then every potential peptide from that protein was extracted. 797

798 Each of the seven algorithms were independently applied  
799 to each of the 52 allele data sets. For each allele data set, the  
800 minimum score threshold was determined for each algorithm  
801 that recovered 50% of the allele repertoire size (the total num-  
802 ber of target peptides observed in the MS data set for that allele).  
803 Additionally, the expected accuracy of each algorithm was as-  
804 sessed by calculating the observed false detection rate (the  
805 fraction of identified peptides that were decoy peptides) using  
806 the identified algorithm and allele specific scoring threshold.  
807 The parameterization process was repeated 1000 times for each  
808 allele through bootstrap sampling of half of the peptides in each  
809 single MHC allele data set. The final FDR and score threshold  
810 for each algorithm at each allele was determined by taking  
811 the median value of both quantities reported during bootstrap  
812 sampling.

813 **Peptide confidence assessment.** Peptide confidence is as-  
814 signed by calculating the  $peptide^{FDR}$ . This quantity is de-  
815 fined as the product of the empirical FDRs of each individual  
816 algorithm that detected a given peptide. The  $peptide^{FDR}$  is  
817 calculated using equation 1,

$$peptide^{FDR} = \prod_{i=1, i \neq ND}^N algorithm_i^{FDR} \quad (1)$$

818 , where  $N$  is the number of MHC-I binding and processing algo-  
819 rithms,  $ND$  represents an algorithm that did not detect a given  
820 peptide, and  $algorithm_i^{FDR}$  represents the allele specific FDR  
821 of the  $N$ th algorithm.

822 The  $peptide^{FDR}$  represents the joint probability that all  
823 MHC-I binding and processing algorithms that detected a particu-  
824 lar peptide did so in error, and therefore returns a probability  
825 of false detection. Unless otherwise stated, EnsembleMHC  
826 selected peptides based on the criterion of a  $peptide^{FDR} \leq$   
827 5%.

### 828 Application of EnsembleMHC to tumor cell line data

829 **Tumor MHC-I peptide data sets.** Ten tumor samples were  
830 obtained from the *Sarkizova et al.* data sets. Tumor samples  
831 were selected for analysis if at least 50% of the expressed MHC-  
832 I alleles for that sample were included in the 52 MHC-I alleles  
833 supported by EnsembleMHC. For each data set, decoy peptides  
834 were generated in a manner identical to the method used for  
835 algorithm parameterization on single MHC allele data.

836 **Tumor MHC-I peptide identification.** Peptide identification  
837 by each algorithm was based on restrictive or permissive bind-  
838 ing affinities thresholds. These thresholds correspond to com-  
839 monly used score cutoffs for the identification of strong binders  
840 (restrictive) or all binders (permissive). These thresholds are

841 0.5% (percentile rank) or 50nM (IC50 value) for strong binders, 888  
842 and 2% (percentile rank) or 500nM (IC50 value) for all binders. 889  
843 Due to the lack of recommend score thresholds for MHCflurry- 890  
844 presentation, the raw presentation score was converted to a 891  
845 percentile score by histogramming the presentation scores pro- 892  
846 duced by 100,000 randomly generated peptides. 893

#### 847 **Application of EnsembleMHC for the prediction of** 848 **SARS-CoV-2 MHC-I peptides**

849 **SARS-CoV-2 reference sequence.** MHC-I peptide pre- 894  
850 dictions for the SARS-CoV-2 proteome were performed 895  
851 using the Wuhan-Hu-1(MN908947.3) reference sequence 896  
852 (<https://www.ncbi.nlm.nih.gov/genbank/sars-cov-2-seqs/>). All 897  
853 potential 8-14mer peptides (n= 67,207) were derived from the 898  
854 open reading frames in the reported proteome, and each peptide 899  
855 was evaluated by the EnsembleMHC workflow. 900

856 **SARS-CoV-2 polymorphism analysis and protein struc-** 905  
857 **ture visualizations.** Polymorphism analysis of SARS-CoV-2 906  
858 structural proteins were performed using 102,148 full length 907  
859 protein sequences obtained from the COVDep database<sup>40</sup>. 908  
860 Solved structures for the E (5X29) and S (6VXX) proteins 909  
861 (<http://www.rcsb.org/>)<sup>41</sup> and predicted structures for the M and 910  
862 N proteins<sup>42</sup> were visualized using VMD<sup>43</sup>. 911

#### 863 **Application of EnsembleMHC to determine population** 864 **SARS-CoV-2 binding capacity**

865 The peptides identified by the EnsembleMHC workflow were 912  
866 used to assess the SARS-CoV-2 population binding capacity by 913  
867 weighing individual MHC allele SARS-CoV-2 binding capaci- 914  
868 ties by regional expression (for a schematic representation see 915  
869 SI A.6). 916

870 **Population-wide MHC-I frequency estimates by country.** 917  
871 The selection of countries included in the EnsembleMHC popu- 918  
872 lation binding capacity assessment was based on several criteria 919  
873 regarding the underlying MHC-I allele data for that country (**SI** 920  
874 **A.6**). The MHC-I allele frequency data used in our model was 921  
875 obtained from the Allele Frequency Net Database (AFND)<sup>18</sup>, 922  
876 and frequencies were aggregated by country. However, the 923  
877 currently available population-based MHC-I frequency data 924  
878 has specific limitations and variances, which we have addressed 925  
879 as follows: 926

880  
881 *Quality of MHC data within countries.* We define MHC- 927  
882 typing breadth as the diversity of identified MHC-I alleles 928  
883 within a given country, and its depth as the ability to accurately 929  
884 achieve 4-digit MHC-I genotype resolution. High variability 930  
885 was observed in both the MHC-I genotyping breadth and depth 931  
886 (**SI A.6 inset**). Consequently, additional filter-measures were 932  
887 introduced to capture potential sources of variance within the

analyzed cohort of countries. The thresholds for filtering the 888  
country-wide MHC-I allele data were set based on meeting 889  
two inclusion criteria: 1) MHC genotyping of at least 1000 890  
individuals have been performed in that population, avoiding 891  
skewing of allele frequencies due to small sample size. 2) 892  
MHC-I allele frequency data for at least 51 of the 52 (95%) 893  
MHC-I alleles for which the EnsembleMHC was parameterized 894  
to predict, ensuring full power of the EnsembleMHC workflow. 895

*Ethnic communities within countries.* In instances where 896  
the MHC-I allele frequencies would pertain to more than one 897  
community, the reported frequencies were counted towards 898  
both contributing groups. For example, the MHC-I frequency 899  
data pertaining to the Chinese minority in Germany would 900  
be factored into the population MHC-I frequencies for both 901  
China and Germany. In doing so, this treatment resolves both 902  
ancestral and demographic MHC-I allele frequencies. 903  
904

**Normalization of MHC allele frequency data.** The focus of 905  
this work was to uncover potential differences in SARS-CoV-2 906  
MHC-I peptide presentation dynamics induced by the 52 se- 907  
lected alleles within a population. Accordingly, the MHC-I 908  
allele frequency data was carefully processed in order to main- 909  
tain important differences in the expression of selected alleles, 910  
while minimizing the effect of confounding variables. 911

The MHC-I allele frequency data for a given population 912  
was first filtered to the 52 selected alleles. These allele fre- 913  
quencies were then converted to the theoretical total number 914  
of copies of that allele within the population (*allele count*) 915  
following 916

$$allele\ count = allele_{freq} \times 2 \times n \quad (2)$$

, where  $allele_{freq}$  is the observed allele frequency in a popula- 917  
tion and  $n$  is the population sample size for which that allele 918  
frequency was measured. The allele count is then normalized 919  
with respect to the total allele count of selected 52 alleles within 920  
that population using the following relationship 921

$$norm\ allele\ count_i = \frac{allele\ count_i}{\sum_{i=1}^{52} allele\ count_i} \quad (3)$$

, where  $i$  is one of the 52 selected alleles. This normaliza- 922  
tion is required to overcome the potential bias towards *hidden* 923  
*alleles* (alleles that are either not well characterized or not sup- 924  
ported by EnsembleMHC) as would be seen using alternative 925  
allele frequency accounting techniques (e.g. sample-weighted 926  
mean of selected allele frequencies or normalization with re- 927  
spect to all observed alleles within a population (**SI A.22**)). The 928  
SARS-CoV-2 binding capacity of these *hidden alleles* cannot be 929  
accurately determined using the EnsembleMHC workflow, and 930  
therefore important potential relationships would be obscured. 931

932 **EnsembleMHC population score.** The predicted ability of a  
933 given population to present SARS-CoV-2 derived peptides was  
934 assessed by calculating the EnsembleMHC Population (EMP)  
935 score. After the MHC-I allele frequency data filtering steps, 23  
936 countries were included in the analysis. The calculation of the  
937 EnsembleMHC population score is as follows

$$EMP\ score = \frac{\sum_{i=1}^{52} peptide_{frac} \times norm\ allele\ count_i}{N_{norm\ allele\ count \neq 0}} \quad (4)$$

938 , where *norm allele count* is the observed normalized  
939 allele count for a given allele in a population,  
940  $N_{norm\ allele\ count \neq 0}$  is the number of the 52 select alleles  
941 detected in a given population (range 51-52 alleles), and  
942 *peptide<sub>frac</sub>* is the peptide fraction or the fraction of total  
943 predicted peptides expected to be presented by that allele within  
944 the total set of predicted peptides with a  $peptide^{FDR} \leq 5\%$ .

945 **Death rate-presentation correlation.** The correlation between  
946 the EMP score and the observed deaths per million within  
947 the cohort of selected countries was calculated as a function  
948 of time. SARS-Cov-2 data covering the time dependent  
949 global evolution of the SARS-CoV-2 pandemic was obtained  
950 from Johns Hopkins University Center for Systems Science  
951 and Engineering<sup>44</sup> covering the time frame of January 22nd to  
952 April 9th. The temporal variations in occurrence of community  
953 spread observed in different countries were accounted for by  
954 rescaling the time series data relative to when a certain minimum  
955 death threshold was met in a country. This analysis was  
956 performed for minimum death thresholds of 1-100 total deaths  
957 by day 0, and correlations were calculated at each day sequentially  
958 following day 0 until there were fewer than 8 countries  
959 remaining at that time point. The upper-limit of 100-deaths was  
960 chosen to ensure availability of death-rate data on at least 50%  
961 of the countries for a minimum of 7 days starting following day  
962 0. Additionally, a steep decline in average statistical power is  
963 observed with day 1 death thresholds greater than 100 deaths  
964 (**SI A.23**).

965 The time death correlation was computed using Spearman's  
966 rank correlation coefficient (two-sided). This method was  
967 chosen due to the small sample size and non-normality of  
968 the underlying data (**SI A.24**). The reported correlations  
969 of EMP score and deaths per million using other correlation  
970 methods can be seen in supplemental figure **SI A.25**.

971 The low statistical power for some of the obtained correlations  
972 were addressed by calculating the Positive Predictive Value  
973 (PPV) of all correlations using the following equation<sup>45</sup>

$$PPV = \frac{1 - \beta \times R}{1 - \beta \times R + \alpha} \quad (5)$$

974 , where  $1 - \beta$  is the statistical power of a given correlation,  
975  $R$  is the pre-study odds, and  $\alpha$  is the significance level. A PPV

value of  $\geq 95\%$  is analogous to a p value of  $\leq 0.05$ . Due to an  
976 unknown pre-study odd (probability that probed effect is truly  
977 non-null),  $R$  was set to 1 in the reported correlations. The proportion  
978 of reported correlations with a PPV of 95% at different  
979  $R$  values can be seen in supplemental figure **SI A.17**. The significance  
980 of partitioning high risk and low risk countries based  
981 on median EMP score was determined using Mann-Whitney  
982 U-test. Significance values were corrected for multiple tests  
983 using the Benjamini-Hochberg procedure<sup>30</sup>.  
984

985 **Sub-sampling of peptides from the Full SARS-CoV-2 proteome.** 108 unique peptides,  
986 derived from the Full SARS-CoV-2 proteome and passing the 5%  $peptide^{FDR}$   
987 filter, were randomly sampled. Then, the time series EMP score - death  
988 per million correlation analysis used to generate **Figure 3** was  
989 applied to each sampled peptide set. The sub-sampling procedure  
990 was repeated for 1,000 iterations (**SI A.18A**). To quantitatively  
991 describe the similarity of the distributions, the Kullback-Leibler  
992 divergence (KLD), a measure of divergence between two probability  
993 distributions, was calculated for the correlation distribution of each  
994 sub-sample iteration relative to either the correlation distribution  
995 of the Full SARS-CoV-2 proteome or SARS-CoV-2 structural proteins  
996 (**SI A.18B**).  
997

#### 998 **Analysis of additional SARS-CoV-2 risk factors**

999 **Additional SARS-CoV-2 risk factors.** Twelve potential SARS-CoV-2  
1000 risk factors (**table B.4**) were selected for analysis. Country-specific  
1001 data for each risk factor was obtained from the Global Health  
1002 Observatory data repository provided by the World Health Organization  
1003 (<https://apps.who.int/gho/data/node.main>). Countries were  
1004 selected for analysis based on the criteria of having reported  
1005 data in the WHO data sets and inclusion in the set of 23 countries  
1006 for which EnsembleMHC population scores were assigned  
1007 (**table B.4A**). Data regarding the total number of noncommunicable  
1008 disease-related deaths (Cardiovascular disease, Chronic obstructive  
1009 pulmonary disease, and Diabetes mellitus) were converted to deaths  
1010 per million.  
1011

1012 **Correlation of additional risk factors with observed deaths per million.**  
1013 Correlation analysis of each additional factor was carried out in a  
1014 similar manner to that of the EnsembleMHC population score. In  
1015 short, Spearman's correlation coefficient between each individual  
1016 factor and observed deaths per million was estimated as a function  
1017 of time from when a specified minimum death threshold was met  
1018 (**Figure 4**). The significance level was set to  $p \leq 0.05$  and  
1019 significant PPV was set to  $PPV \geq 0.95$  (eq 8).  
1020

1021 **Linear models of SARS-CoV-2 mortality.** For the single and  
1022 combination models, individual linear models were constructed  
1023 for each considered death threshold as a function of time (similar  
1024 to the univariate correlation analysis). Each model consisted



1025 of 1 (a single socioeconomic or health-related risk factor) or 2 (a  
1026 combination of 1 risk factor and structural protein EMP score)  
1027 dependent variables and deaths per million as the independent  
1028 variable. The adjusted  $R^2$  value and statistical significance  
1029 of the model (F-test) were then extracted from each individ-  
1030 ual model and aggregated by dependent variable (**figure 4, SI**  
1031 **A.21**).

1032 The best performing models were determined by assess-  
1033 ing all possible combinations of factors including structural  
1034 protein EMP score. This resulted in the consideration of 4,083  
1035 different linear models. The top performing models were then  
1036 selected by ranking each model by median adjusted  $R^2$ .

#### 1037 **Code and data availability.**

1038 All data analysis and statistical tests were performed using the  
1039 R Statistical Computing Environment v.3.6.0 ([http://www.r-](http://www.r-project.org)  
1040 [project.org](http://www.r-project.org)). Data sets and example code are avail-  
1041 able at [https://github.com/eawilson-CompBio/EnsembleMHC-](https://github.com/eawilson-CompBio/EnsembleMHC-Covid.git)  
1042 [Covid.git](https://github.com/eawilson-CompBio/EnsembleMHC-Covid.git)

## **A Supplemental figures: Total predicted MHC-I epitope load is inversely associated with population mortality from SARS-CoV-2**

**Eric Wilson, Gabrielle Herneise, Abhishek Singharoy, Karen S Anderson**

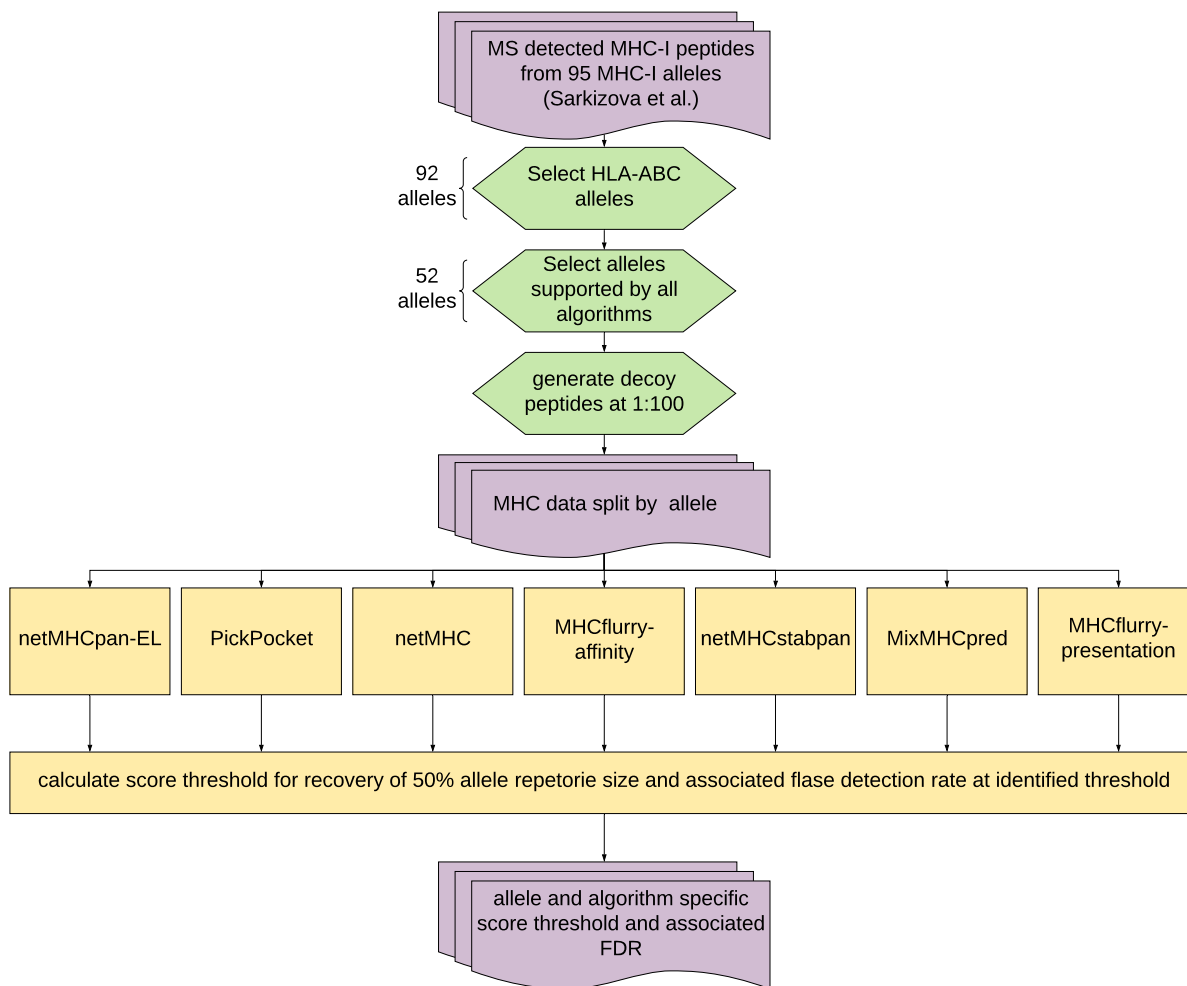
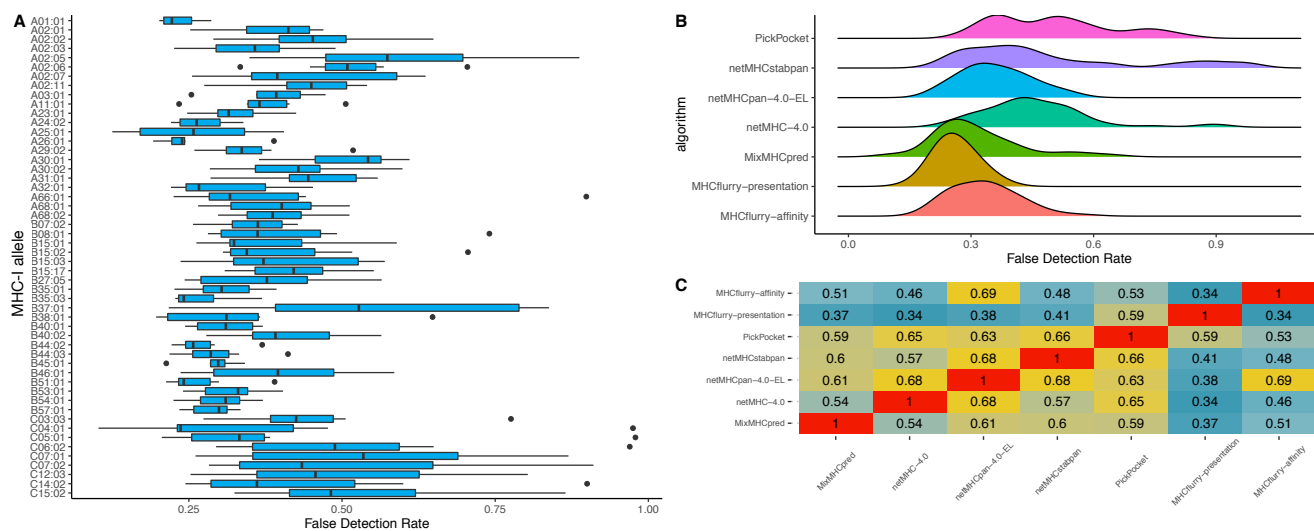


Figure A.1: EnsembleMHC Parameterization overview



**Figure A.2: EnsembleMHC prediction workflow.** **A**, The EnsembleMHC score algorithm was parameterized using high quality mass spectrometry-detected MHC-I peptides paired with a 100-fold excess of randomly generated decoy peptides. Each bar represents the distribution of algorithm-specific false detection rates ( $n = 7$ ) at that MHC allele. Each box plot is in the style of Tukey. **B**, a density plot of the observed FDRs for each algorithm across all alleles ( $n = 52$ ). **C**, The correlation between individual peptide scores for each algorithm across all alleles was calculated using Pearson correlation. Warmer colors indicate a higher level of correlation while cooler colors indicate lower correlation.

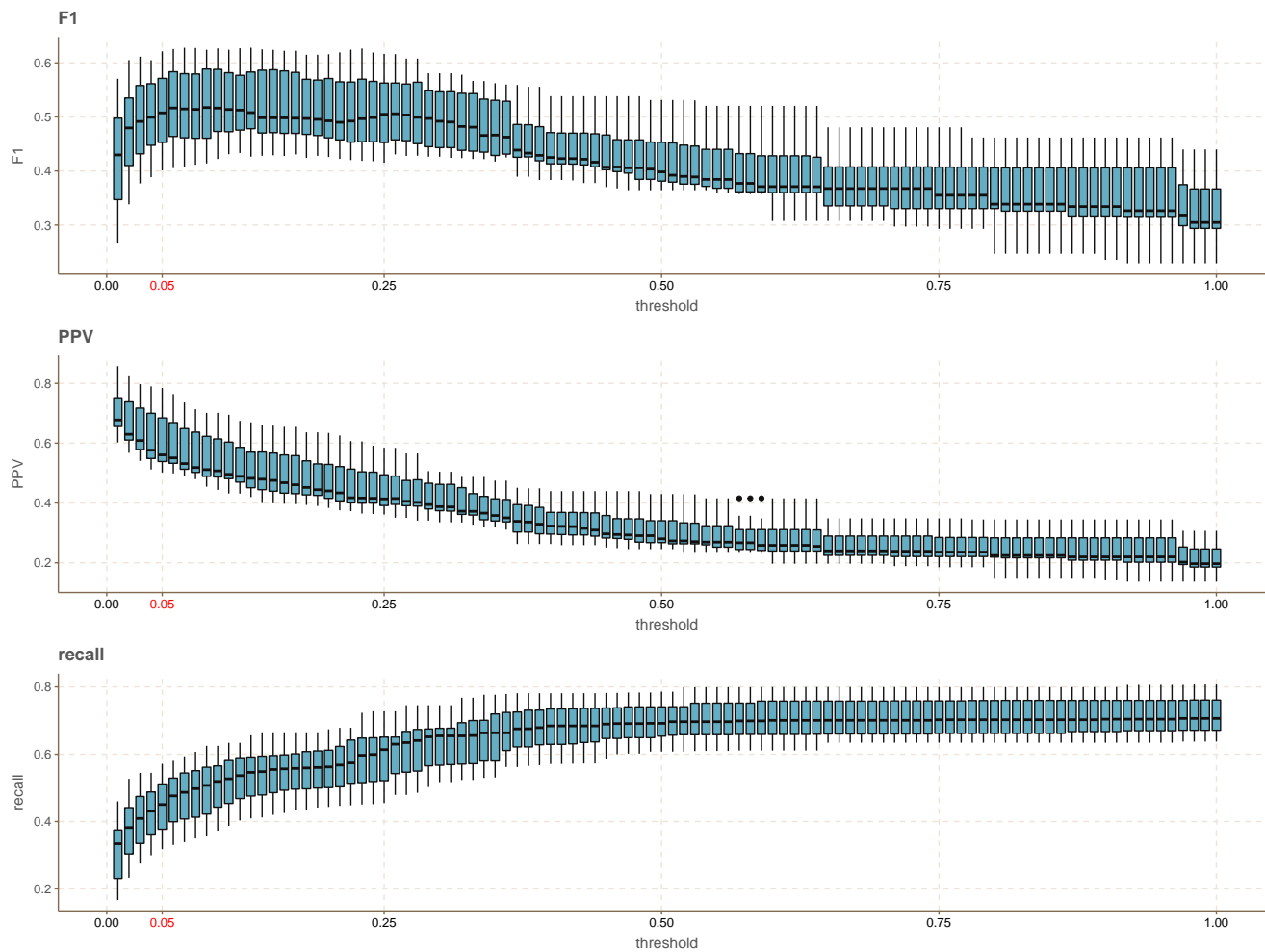


Figure A.3: **The effect of different peptide FDR threshold levels.** The effect of different  $peptide^{FDR}$  cutoff thresholds on the results reported in figure 1 was evaluated for a range of 0.01-1. The  $peptide^{FDR}$  selected for use in this study is highlighted in red.

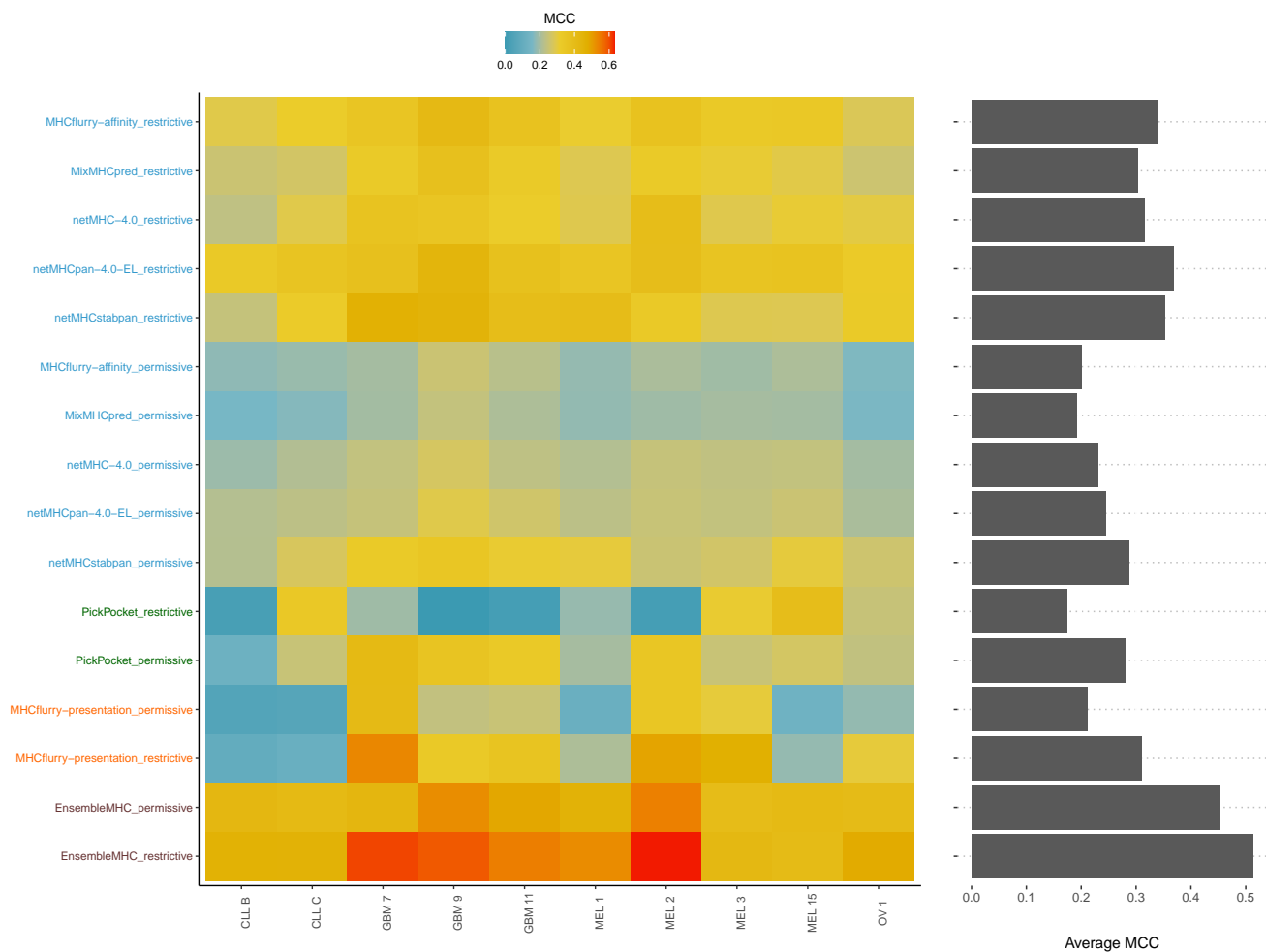


Figure A.4: **Evaluation of individual algorithms using Matthew's correlation coefficient.** As an alternative to F1 score (Figure 1B), Matthew's correlation coefficient was calculated for each algorithm. Warm colors indicate higher MCC while cooler colors indicate lower MCC. The average MCC for each algorithm is represented by the margin bar plot on the right.

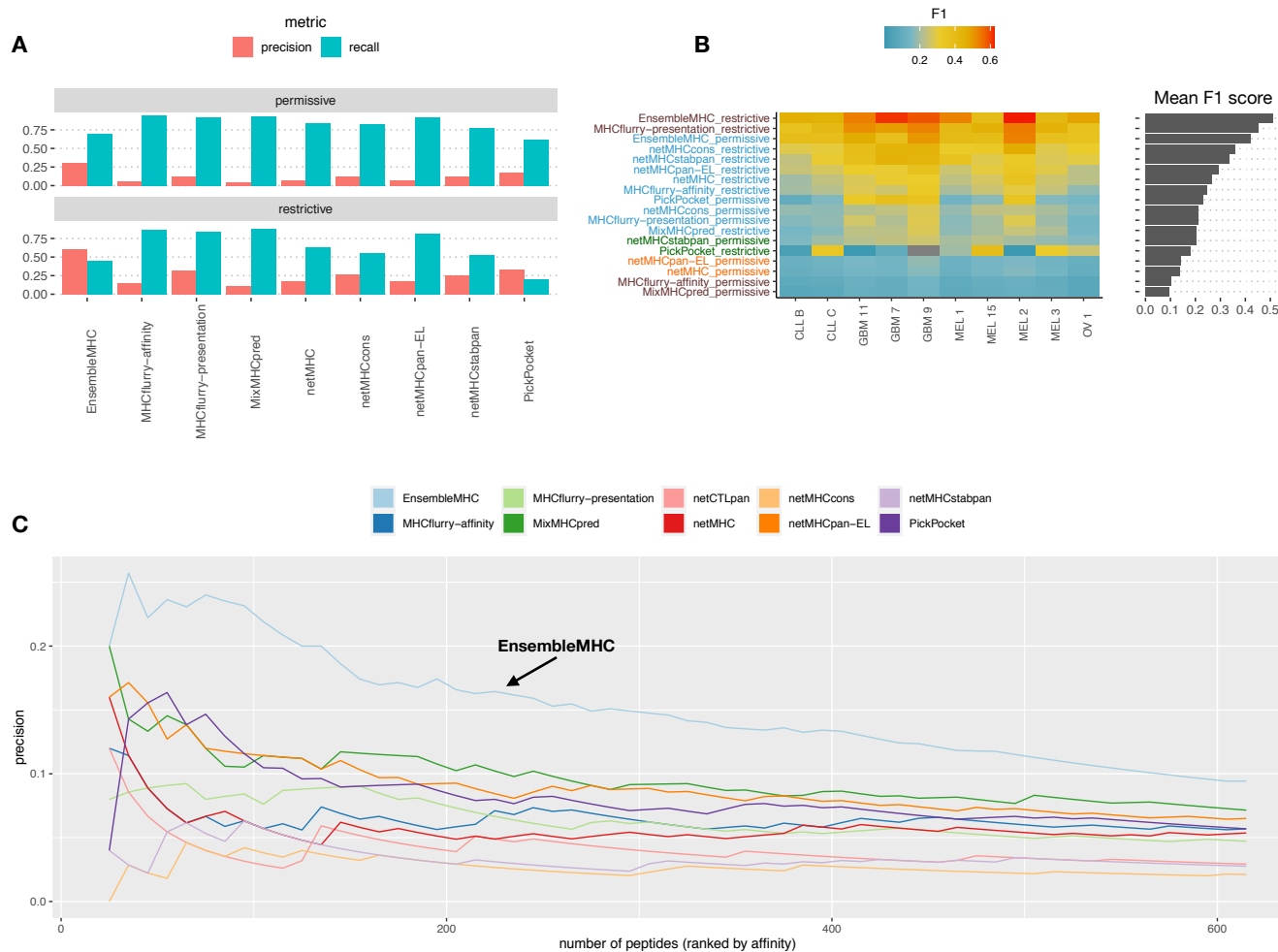


Figure A.5: **Prediction of viral immunogenic epitopes across ensemble-based algorithms.** A-B, The results in reported **figure 1 (A-B)** were compared across ensemble-based MHC-I prediction algorithms. C, The positive predictive value (precision) of the algorithms to select immunogenic MHC-I peptides was assessed across Hepatitis-C genome polyprotein (P26664), Dengue virus genome polyprotein (P14340), and the HIV-1 POL-GAG protein (P03369). All potential 8 – 14mer peptides were extracted from each protein and the resulting peptides were checked against the Immune Epitope database to identify peptides with experimentally validated immunogenicity. The result of this analysis was the generation of a data set comprised of 616 experimentally validated immunogenic peptides and 54,663 putative non-immunogenic peptides. The performance of each algorithm was then assessed by calculating the precision when selecting n number of top scoring peptides as determined by a given algorithm. Precision was calculated for each algorithm across a range of  $n = 25$  to  $n = 615$ .

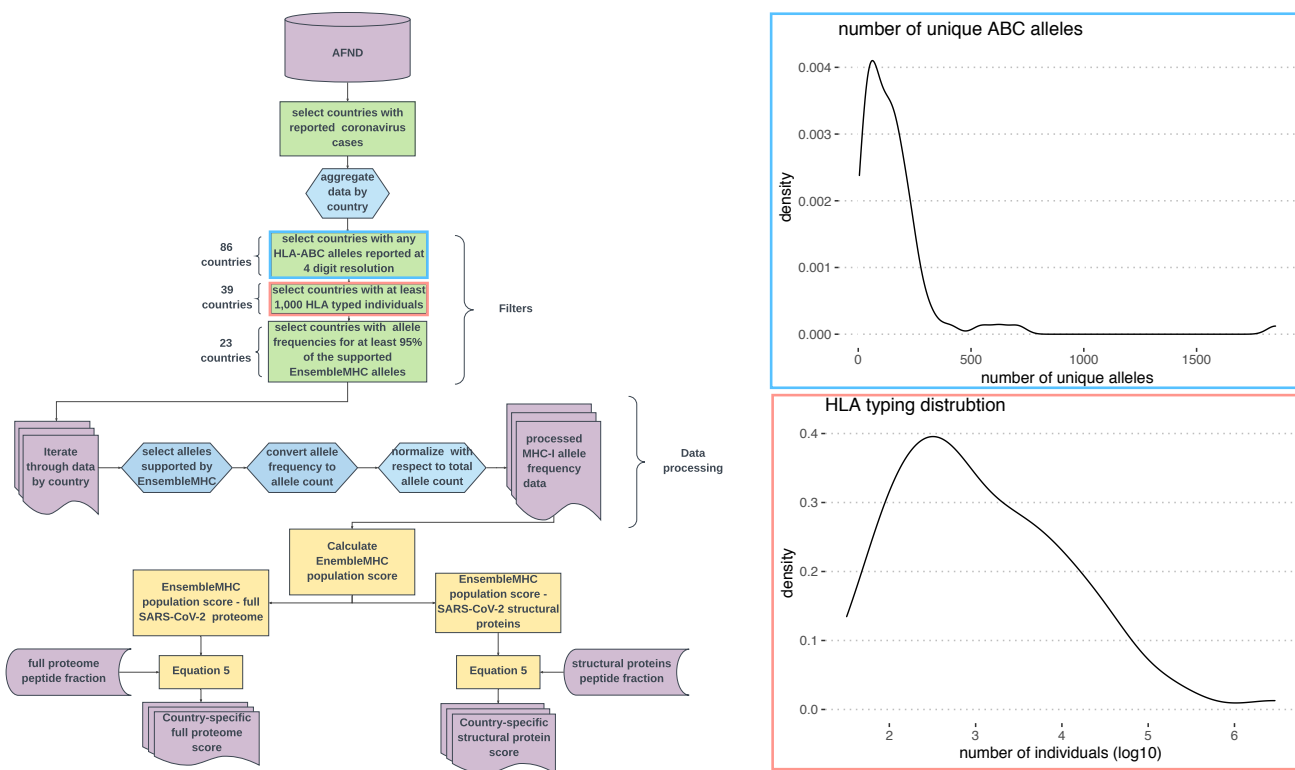


Figure A.6: **Data processing EnsembleMHC population score calculation.** The overview of the data processing steps for the global MHC-I allele frequency data and its application in the calculation the EnsembleMHC population score with respect to the full SARS-CoV-2 proteome and SARS-CoV-2 structural proteins. (inset plots), The blue inset plot illustrates MHC-typing breadth and depth variation by showing the distribution of the total number of MHC-I alleles reported at 4-digit resolution in 86 countries. The red inset plot shows the distribution of the number of MHC-genotyped individuals in the set of countries with at least 1 reported coronavirus case. **AFND = Allele Frequency Net Database**



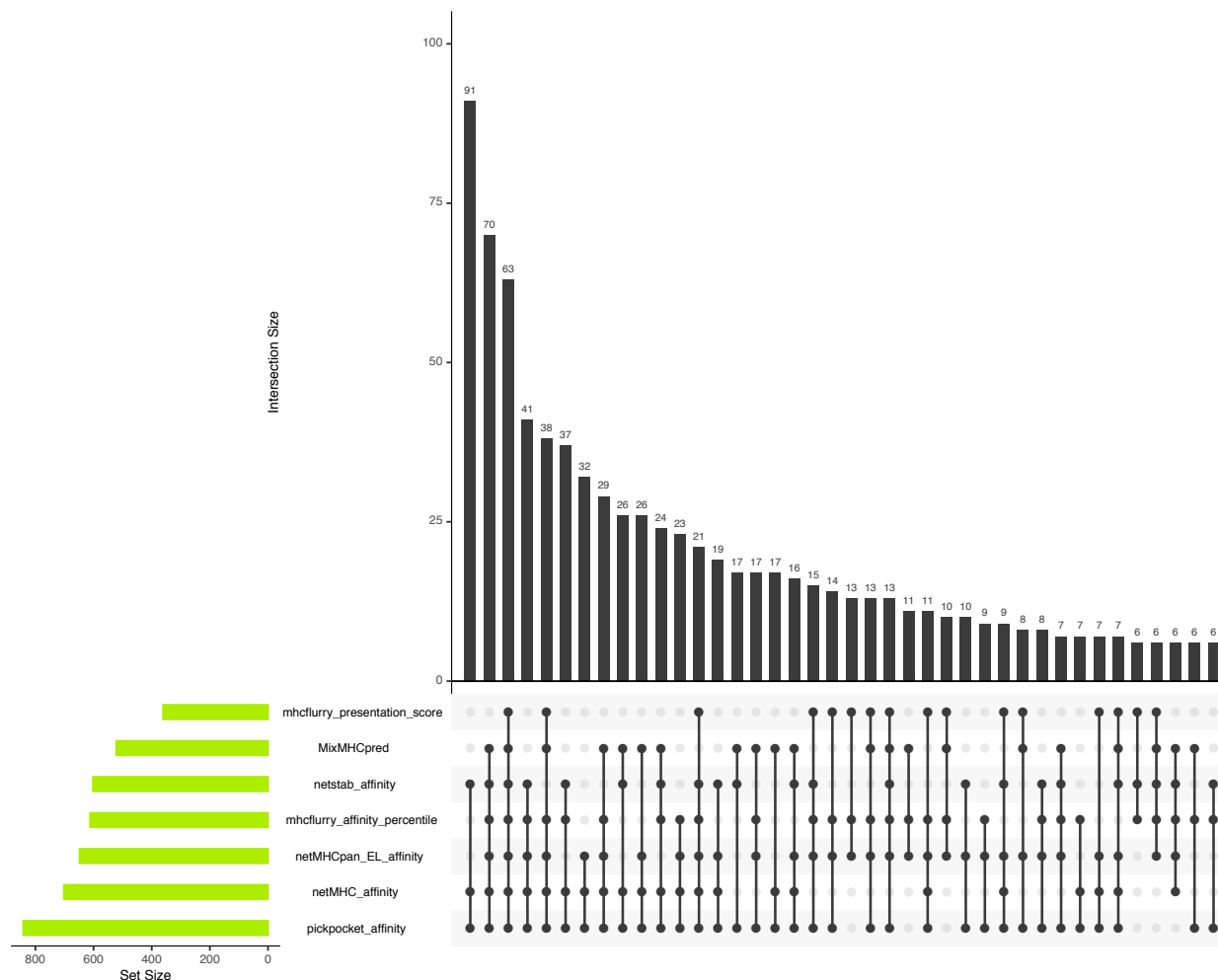


Figure A.7: **Contribution of each EnsembleMHC component algorithm to peptide selection for predicted SARS-CoV-2 peptides.** The UpSet plot shows the contribution of each individual component algorithm to the 658 unique SARS-CoV-2 peptides identified by EnsembleMHC. The top bar plot indicates the number of unique peptides identified by the combination of algorithms shown by the points and segments located under each bar. The bar plot on the left-hand side of the plot indicates the total number of peptides identified by each algorithm.

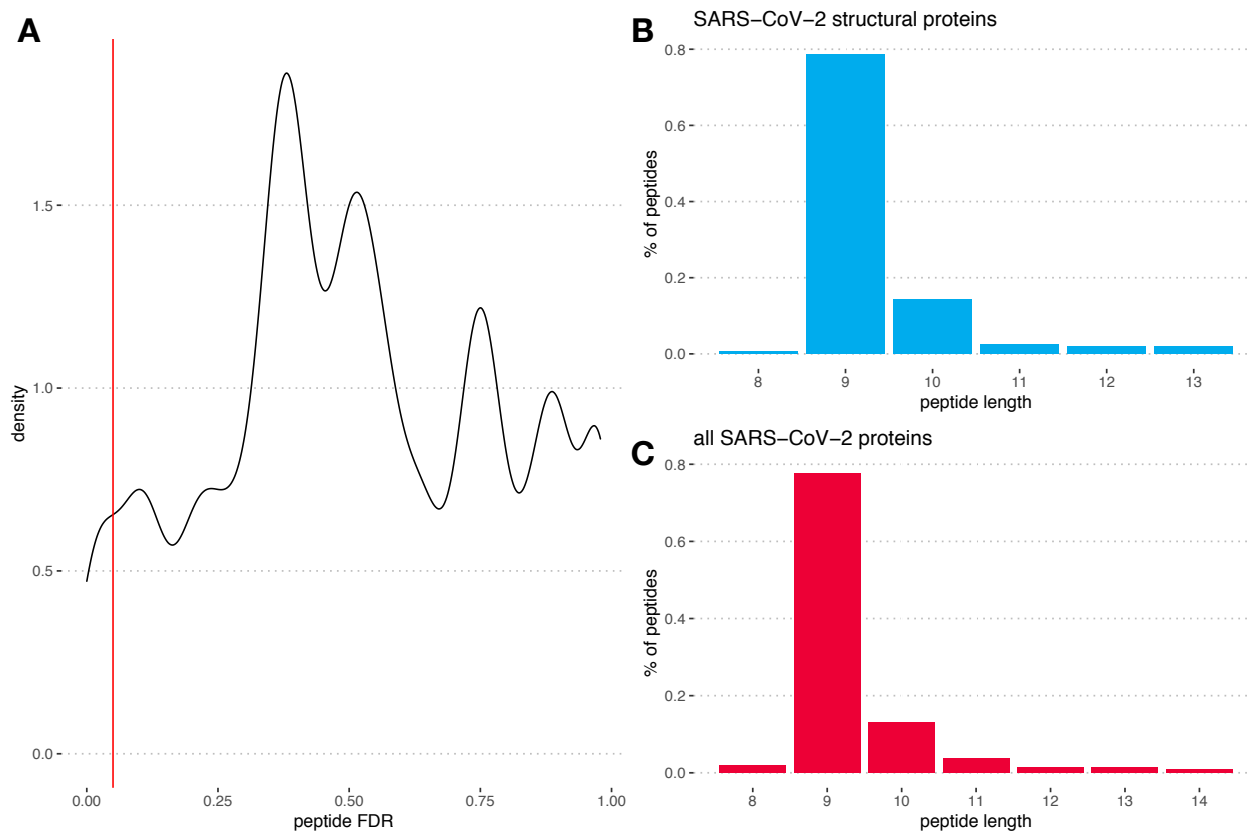
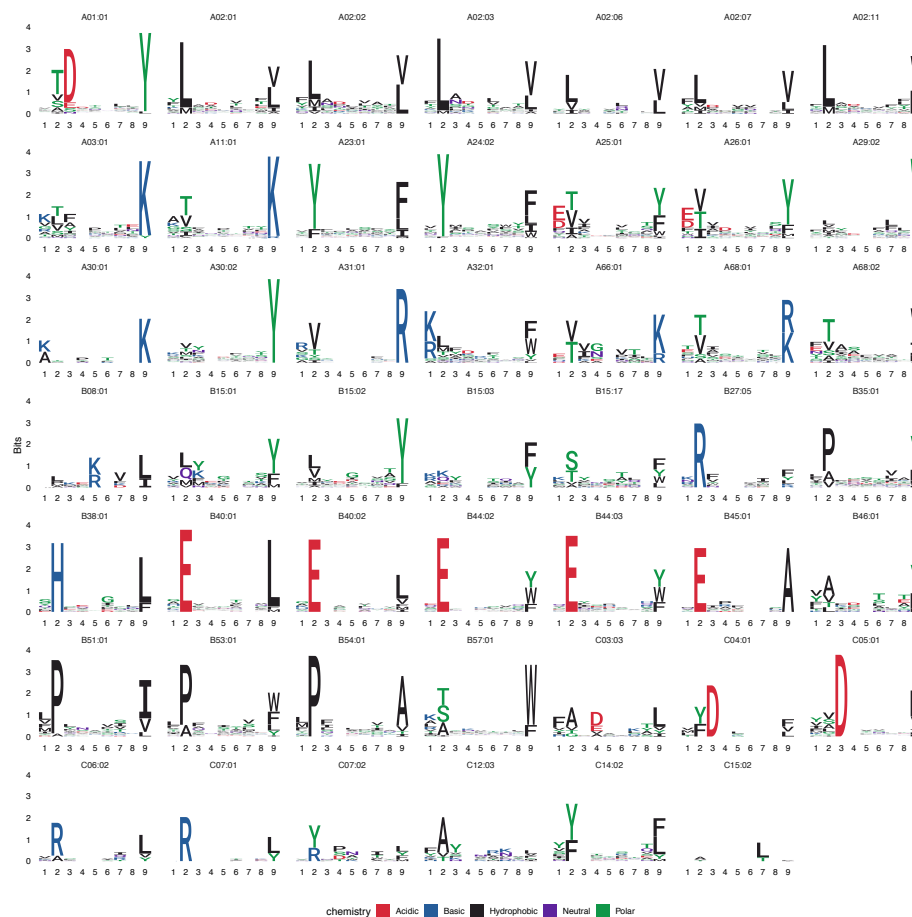


Figure A.8: **EnsembleMHC peptide<sup>FDR</sup> and length distributions of predicted SARS-CoV-2 MHC-I peptides.** **A**, The distribution of the  $peptide^{FDR}$  for 9,712 SARS-CoV-2 peptides that fell with the score threshold of at least one component algorithm. The red line indicates an  $peptide^{FDR}$  level of  $\leq 5\%$ . **B**, The length distribution of the 108 high-confidence peptides identified from SARS-CoV-2 structural proteins. **C**, The length distribution of the 658 high-confidence peptides identified from full SARS-CoV-2 proteome.



**Figure A.9: Logo plots for the identified peptides from the SARS proteome.** Logo plots were generated for MHC alleles with at least 5 peptides identified by EnsembleMHC prediction. Peptides shorter than 9 amino acids had random amino acid inserted into a non-anchor position while peptides longer than 9 amino acids had a random non-anchor position deleted. Large amino acid character height indicates a high frequency of that amino acid at that position. Amino acids are colored residue type.

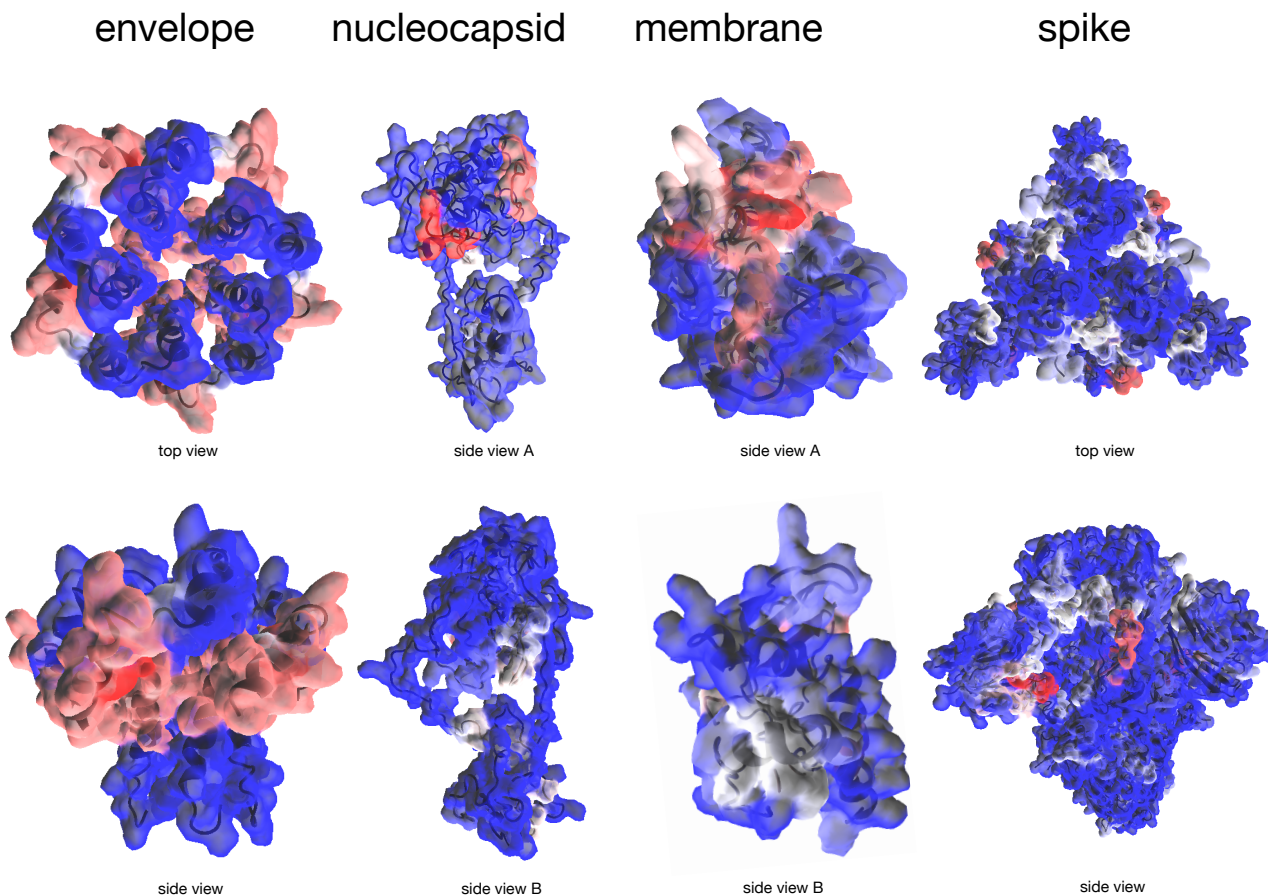


Figure A.10: **Molecular origin of predicted SARS-CoV-2 structural protein MHC-I peptides.** The predicted SARS-CoV-2 structural protein MHC-I peptides were mapped onto the solved structures for the envelope and spike proteins, and the predicted structures for the nucleocapsid and membrane proteins. Red highlighted regions indicate an enrichment of predicted peptides while blue regions indicate a depletion of predicted peptides.

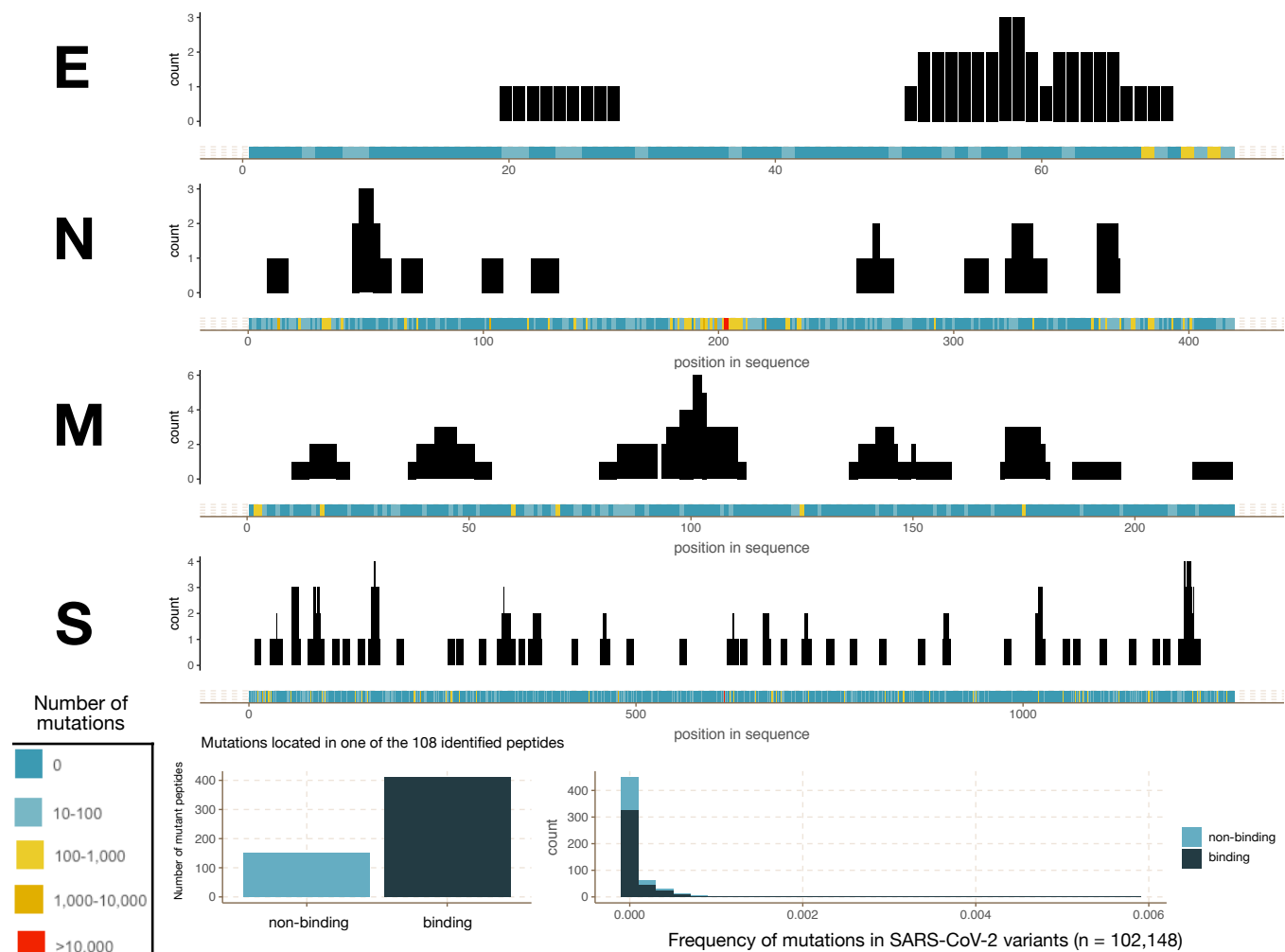
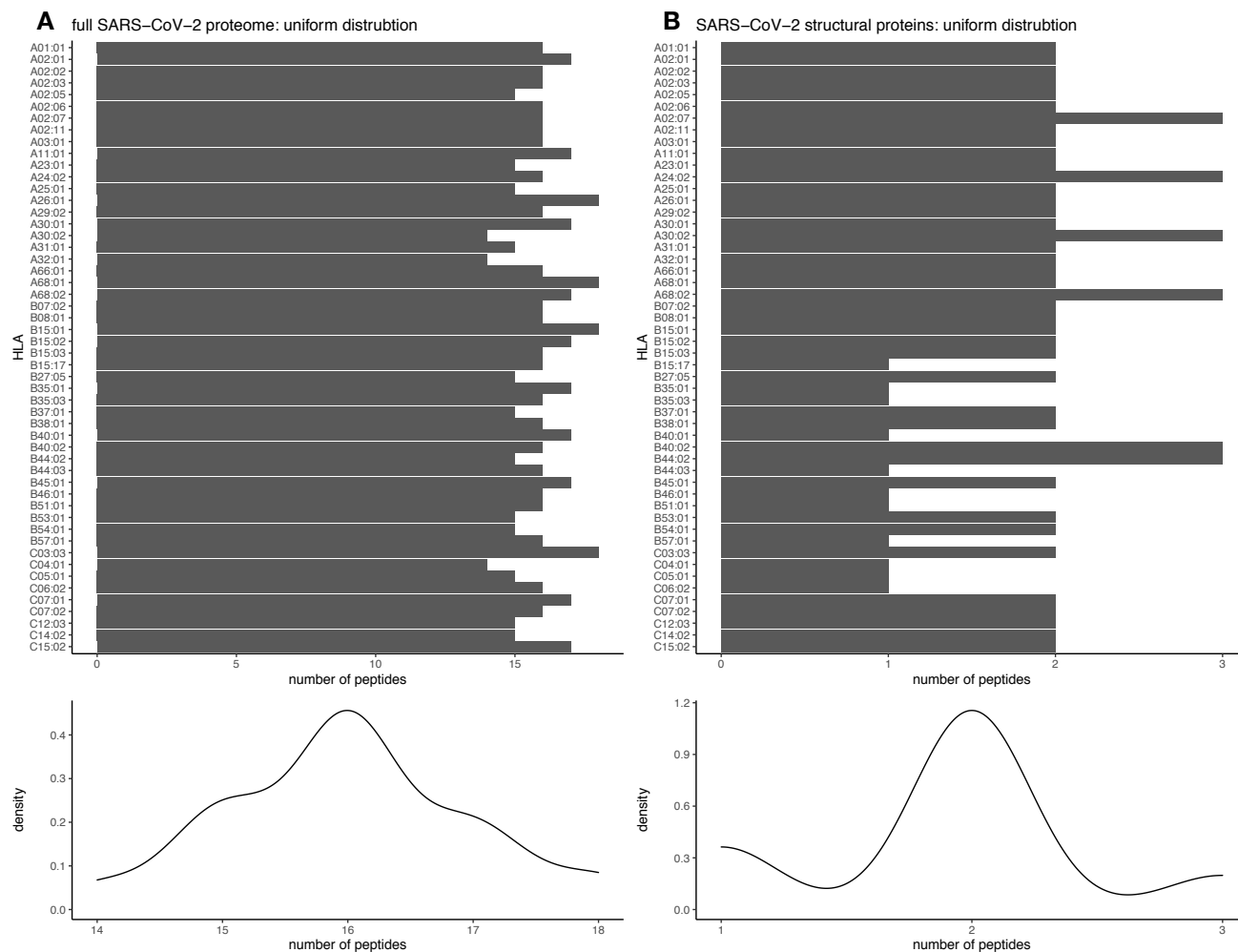


Figure A.11: **Impact of SARS-CoV-2 sequence polymorphism on predicted SARS-CoV-2 structural MHC-I peptides.** Top 4 panels, The incidence of sequence position mutations (colored bar) and the frequency of each amino acid position in one of the 108 SARS-CoV-2 structural protein peptides (black bars) by protein were calculated for 102,148 SARS-CoV-2 sequence variants. Lower left panel, all potential mutations arising in an EnsembleMHC-predicted MHC-I peptides were evaluated for changes in binding affinity ( $peptide^{FDR} > 0.05$ ). Lower right panel, The overall frequency of mutations impacting EnsembleMHC-predicted peptides with light blue indicating deleterious mutations, and dark blue indicating neutral mutations.



**Figure A.12: Simulated even peptide-allele distribution.** The resulting SARS-CoV-2 peptide-MHC allele distribution was compared to an even distribution by means of the Kolmogorov-smirnov test. **A**, An even peptide-allele distribution for the full SARS-CoV-2 proteome was simulated by sampling from a discrete symmetrical distribution centered around the median number of peptides assigned to individual alleles ( $\bar{X} = 16$ ). **B**, An even peptide-allele distribution for the SARS-CoV-2 structural proteins was simulated by sampling from a discrete symmetrical distribution centered around the median number of peptides assigned to individual alleles ( $\bar{X} = 2$ ).

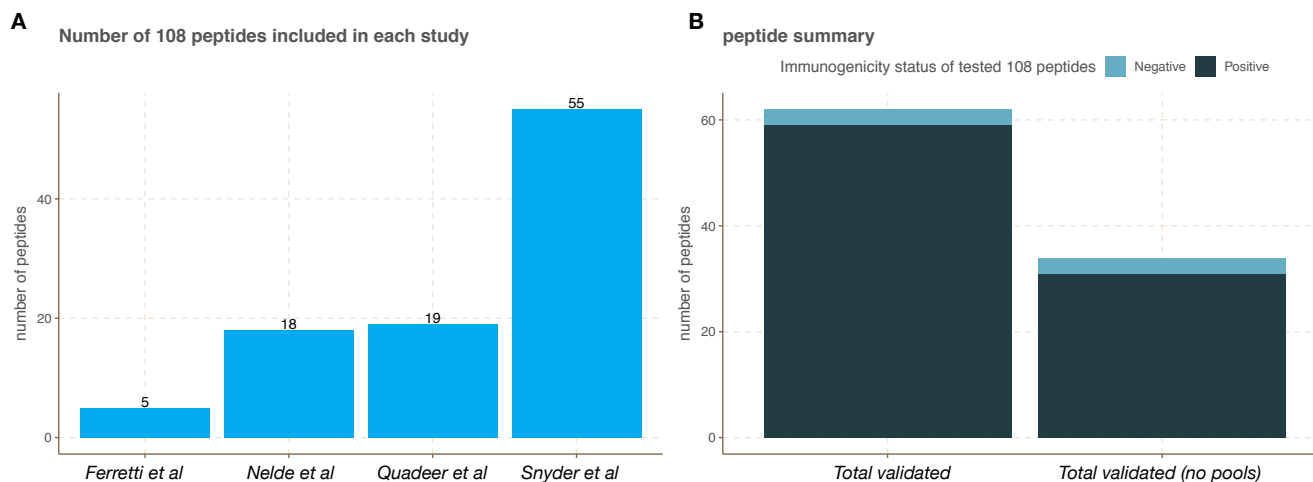


Figure A.13: **External experimental validation of the 108 high confidence SARS-Cov-2 structural protein peptides.** Experimentally validated immunogenic peptides derived from SARS-CoV-2 structural proteins were obtained from 4 independent studies (Ferretti et al<sup>46</sup>, Nelde et al<sup>47</sup>, and Snyder et al<sup>48</sup>) and 1 meta-study (Quadeer et al<sup>49</sup>). These peptides were then assessed for overlap with the 108 SARS-CoV-2 peptides identified by EnsembleMHC (*108 peptides*). **A**, The total number of peptides from the *108 peptides* set that were included for testing in each study. **B**, The summary of immunogenicity status of *108 peptides* across all studies. These summaries were split into two groups. *Total validated* indicates the total number of experimentally validate 108 peptides while *total validated (no pools)* indicates the number of experimentally validated peptides excluding those only tested in peptide pools. This distinction was made due to the potential of peptide pools to obscure which tested peptide is truly responsible for the observed immune response. Overall, 57% of the predicted 108 structural protein peptides were tested with 95% of tested peptides producing an immune response.

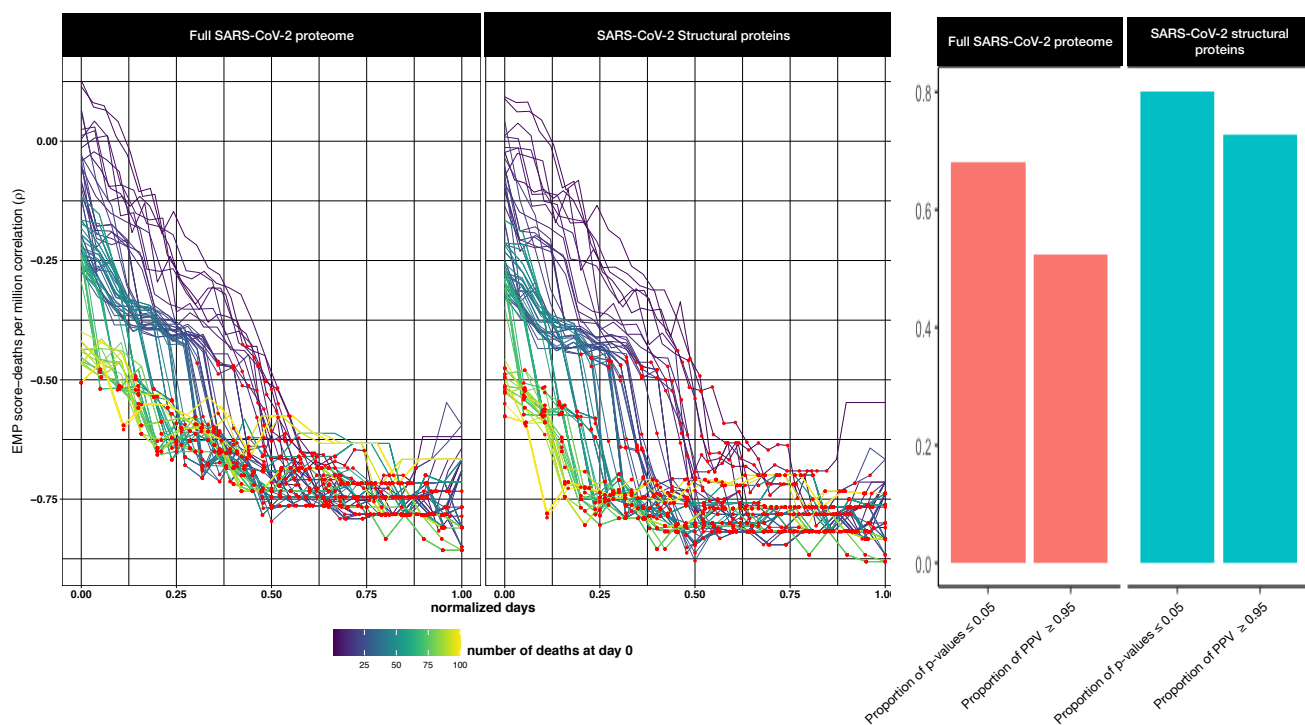


Figure A.14: **Correlation of EMP score based on full SARS-CoV-2 proteome or SARS-CoV-2 structural proteins with observed deaths per million.** **A**, The correlations between EnsembleMHC population score based on the full SARS-CoV-2 proteome (**left**) or EnsembleMHC population score based on SARS-CoV-2 structural proteins (**right**). **B**, The difference in the proportions of significant p-values and PPV between the full SARS-CoV-2 proteome (**left**) and SARS-CoV-2 structural proteins (**right**) (not corrected for multiple testing).



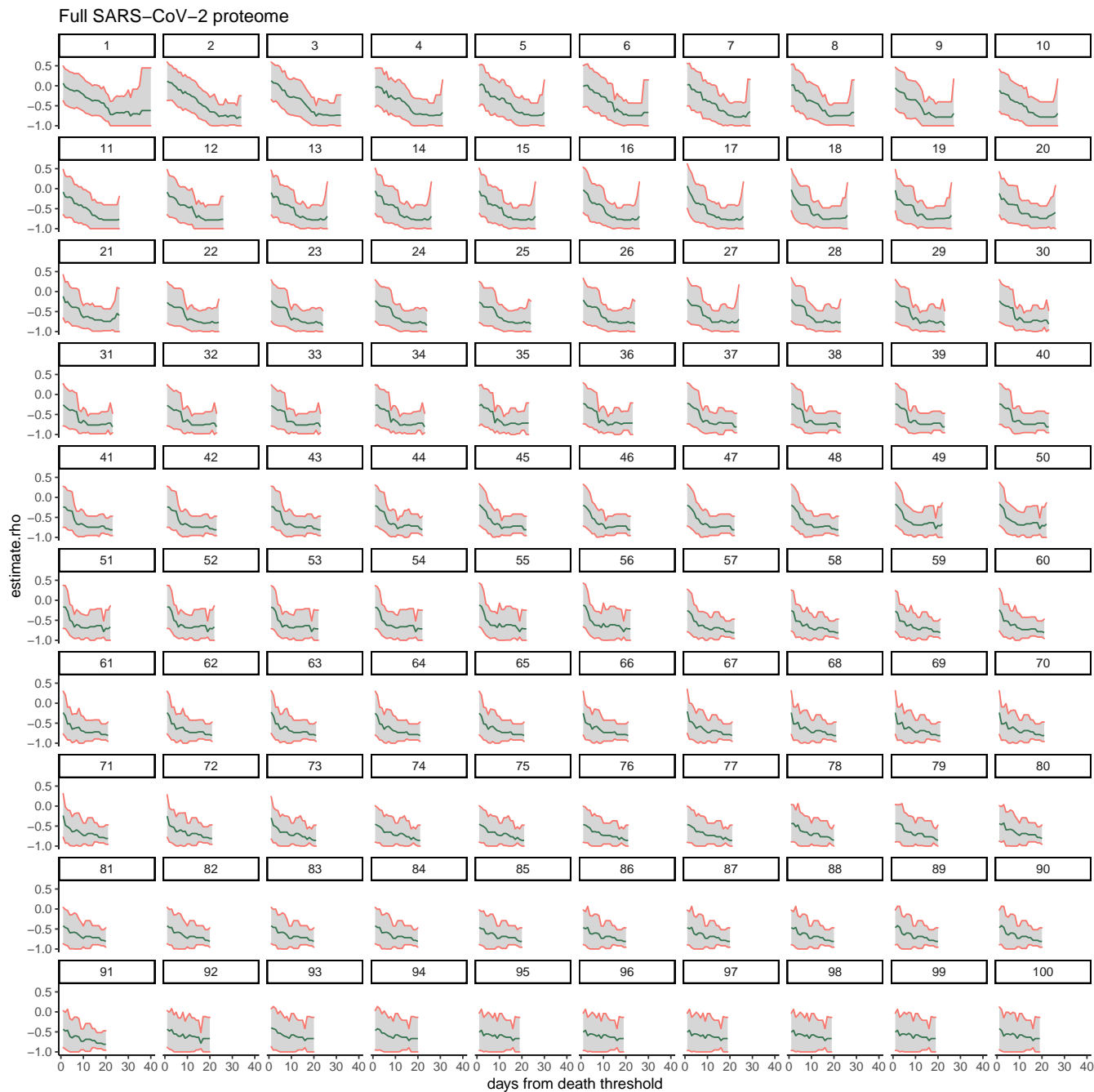


Figure A.15: **95% Confidence interval for the correlations between the EnsembleMHC score based on the full SARS-CoV-2 proteome and observed deaths per million.** Each individual plot shows the 95% confidence interval (grey region) for the correlations between EMP scores based on the full SARS-CoV-2 proteome and observed deaths per million (blue line) for all starting minimum death thresholds (indicated by number above plot).

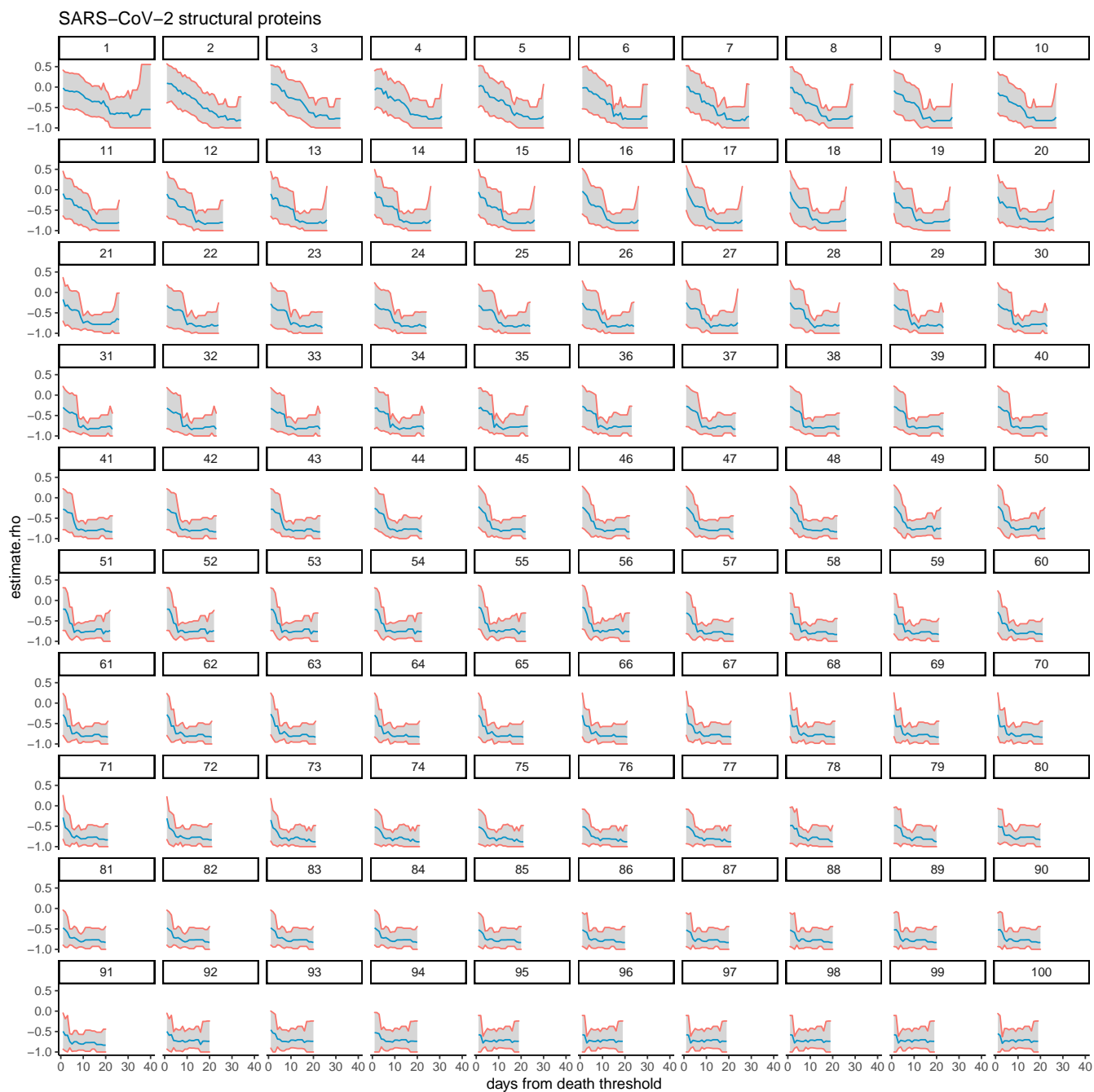


Figure A.16: **95% Confidence interval for the correlations between the EnsembleMHC score based on SARS-CoV-2 structural proteins and observed deaths per million.** Each individual plot shows the 95% confidence interval (grey region) for the correlations between EMP scores based on SARS-CoV-2 structural proteins and observed deaths per million (blue line) for all starting minimum death thresholds (indicated by number above plot).

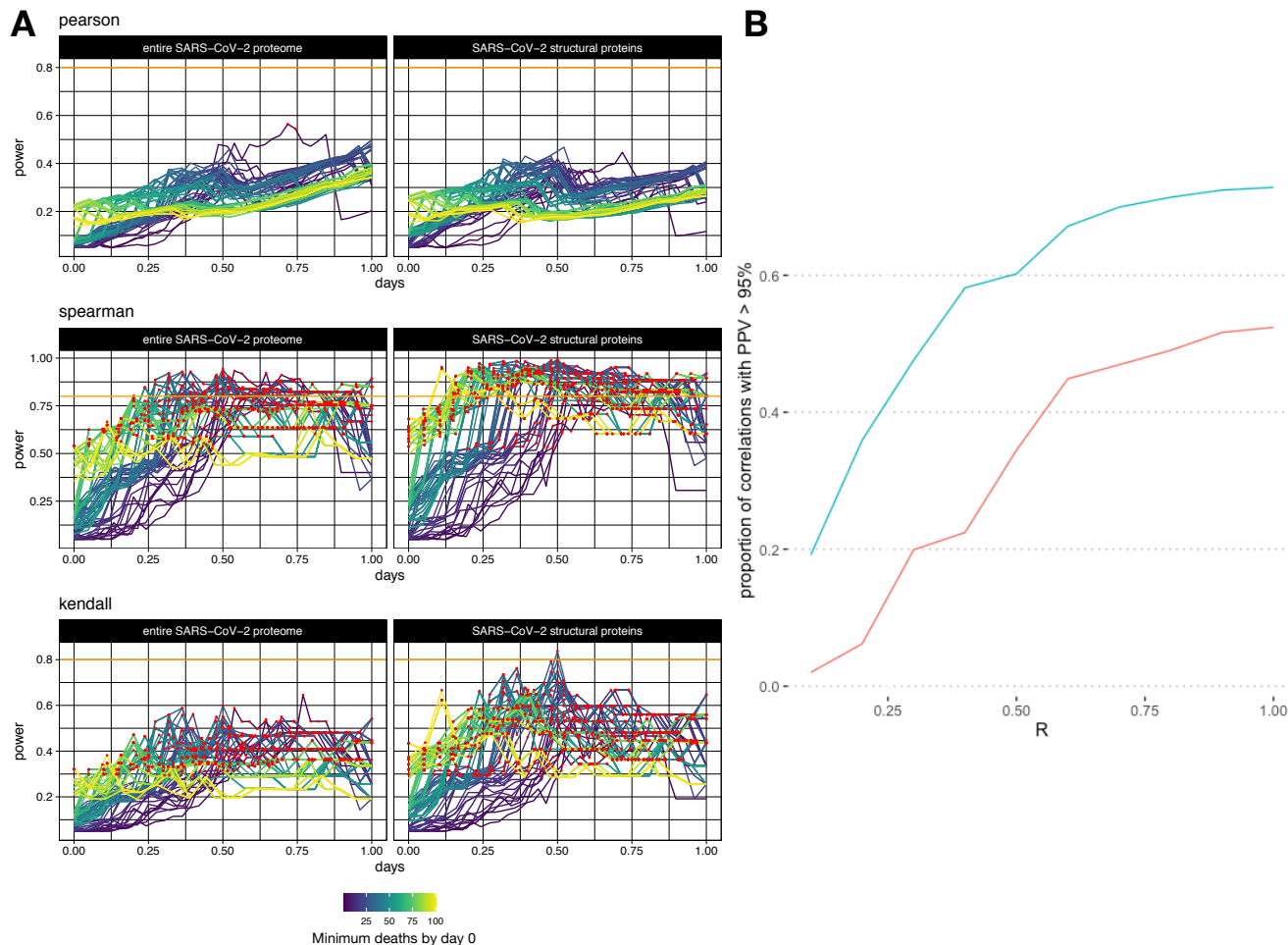
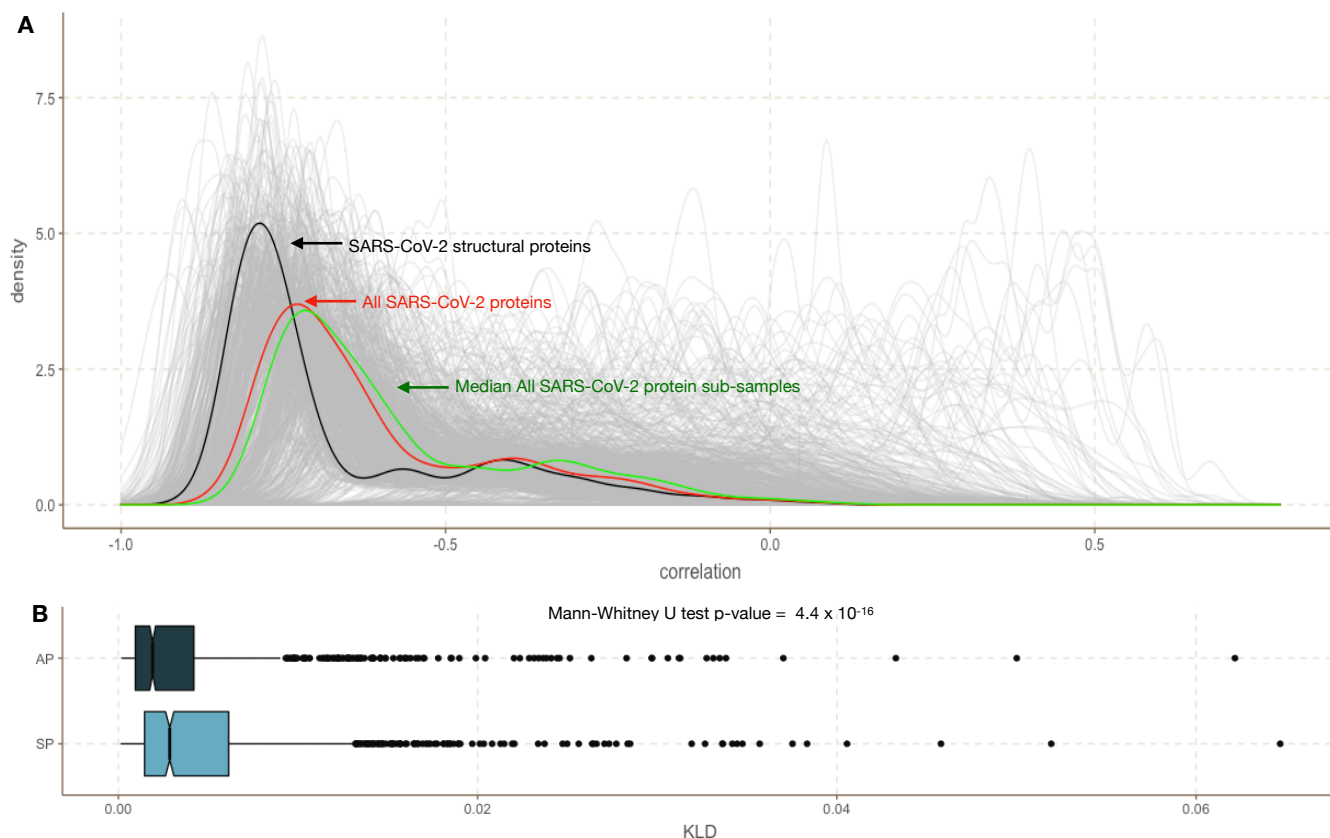


Figure A.17: **Analysis of statistical power for different correlation methods.** **A**, The statistical power of each reported correlation between EnsembleMHC population score with respect to the full SARS-CoV-2 proteome (left column) or specifically structural proteins (right column) and deaths per million were calculated at each day starting from the day a country passed a particular minimum death threshold using Pearson's correlation (**top**), Spearman's rho (**middle**), and Kendall's tau (**bottom**). The days from each start point were normalized, and correlations that were shown to be statistically significant are colored with a red point. The orange line indicates a power threshold of 80%. **B**, The line plot on the right shows the proportion of points achieving a significant PPV at different thresholds for pre-study odds (R) for the spearman correlation carried out in section 3. The blue line represents the proportion of significant correlations for EnsembleMHC score based on SARS-CoV-2 structural proteins while the red line represents the same correlations with an EnsembleMHC population score based on the full SARS-CoV-2 proteome.



**Figure A.18: The effect of sub-sampling EnsembleMHC-identified MHC-I peptides derived from the full SARS-CoV-2 proteome on EMP score - deaths per million correlation distribution.** The robustness of the observed distinction between the EMP score - deaths per million correlation distributions between SARS-CoV-2 structural proteins and all SARS-CoV-2 proteins was assessed by performing sub-sampling of non-structural SARS-CoV-2 MHC-I peptides. **A**, 1,000 sub-sampling iterations were performed by randomly selecting 108 peptides from the full SARS-CoV-2 proteome that passed the 5%  $peptide^{FDR}$  filter. The correlation between the population EMP score produced by each sub-sampled set of peptides and observed deaths per million were plotted (grey lines). The correlation distribution observed for identified SARS-CoV-2 structural protein peptides (black line), all SARS-CoV-2 proteins (red line), and the median correlation distribution across all subsampling iterations (green line) were plotted for comparison. **B**, Kullback-Leibler divergence was calculated for the correlation distribution of each down sample iteration relative to either the correlation distribution of the all peptide group (AP) or the structural peptide group (SP).

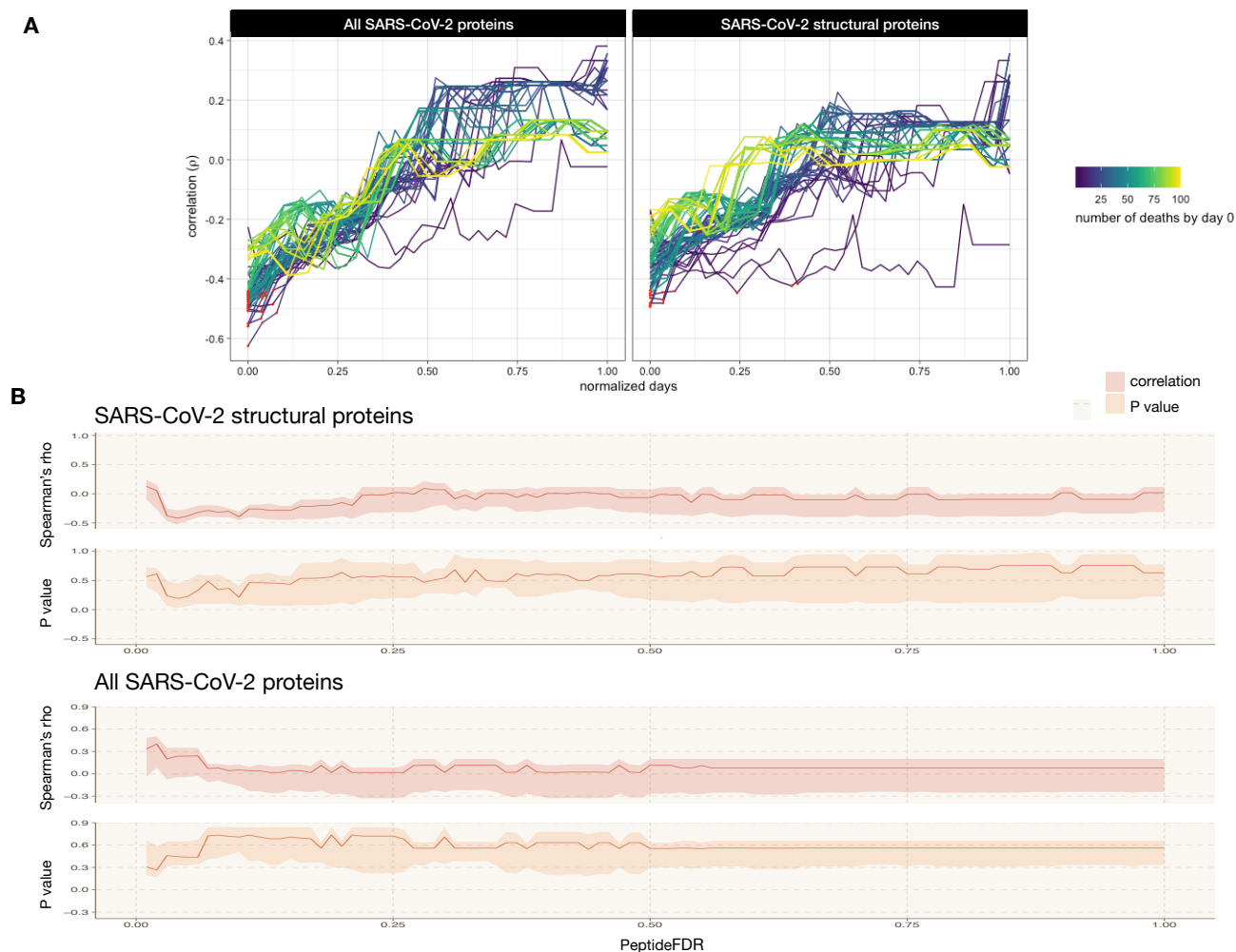


Figure A.19: **The effect of MHC shuffling on the correlation of EMP score and deaths per million.** **A**, The MHC-I allele assessment of peptides that passed an individual algorithm binding affinity thresholds were shuffled prior to  $peptide^{FDR}$  filtering. The red points indicate correlations with a p-value  $\leq 5\%$ . **B**, The impact of varying  $peptide^{FDR}$  cutoff threshold on the shuffled MHC data set. For each  $peptide^{FDR}$  cutoff threshold (x-axis), the upper bound of the shaded region indicates the 75<sup>th</sup> percentile, the lower bound indicates the 25<sup>th</sup> percentile, and the solid line indicates the median.

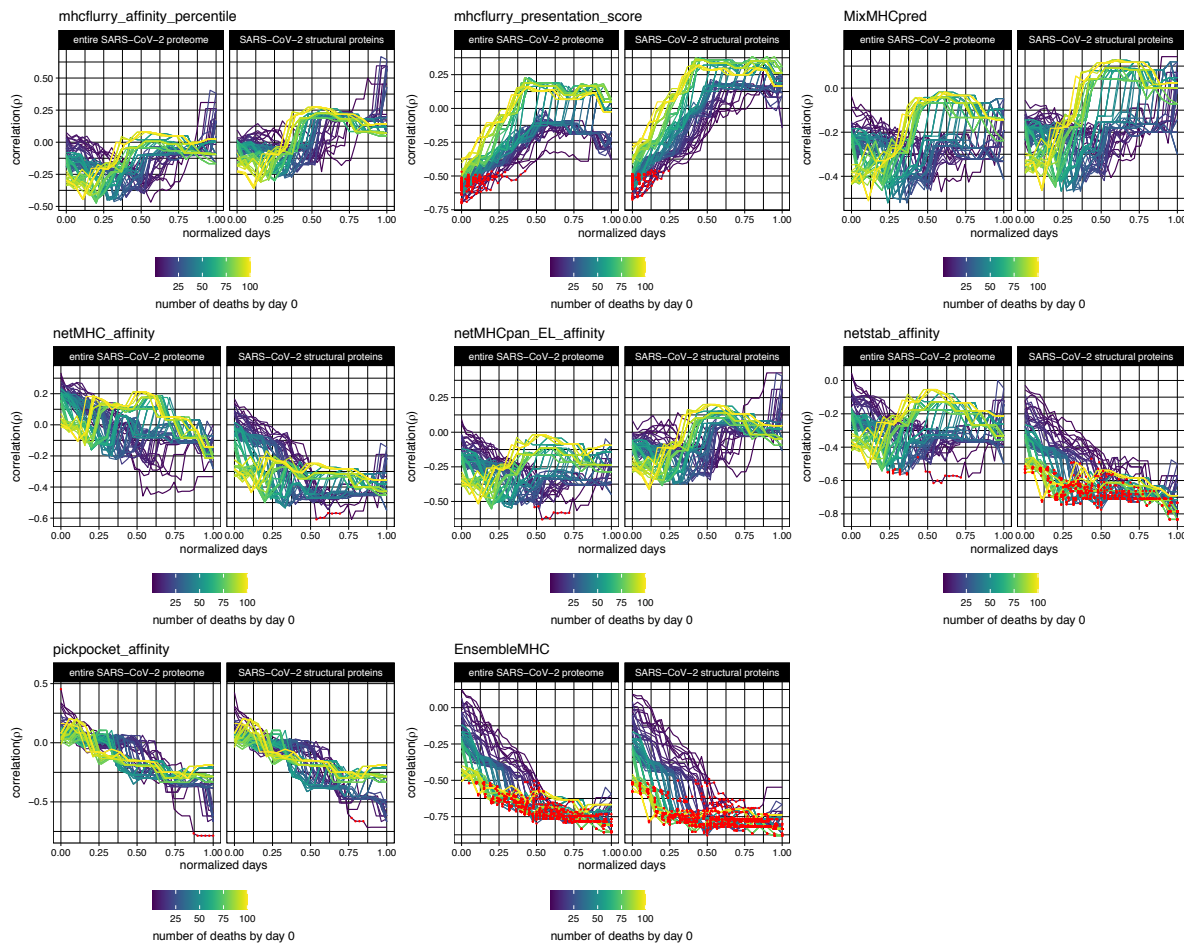


Figure A.20: **Individual algorithms are unable to fully recreate the correlation with population mortality reported by EnsembleMHC.** Population SARS-CoV-2 binding capacities using only single algorithms were correlated to observed deaths per million. For each algorithm, the population SARS-CoV-2 binding capacity was calculated from the resulting viral peptide-MHC allele distribution using restrictive MHC-I binding affinity cutoffs ( $\leq 0.5\%$  for binding percentile scores, top 0.5% MHCflurry presentation score, and  $\leq 50nm$  for PickPocket). Red points indicate a PPV  $\geq 95\%$ .

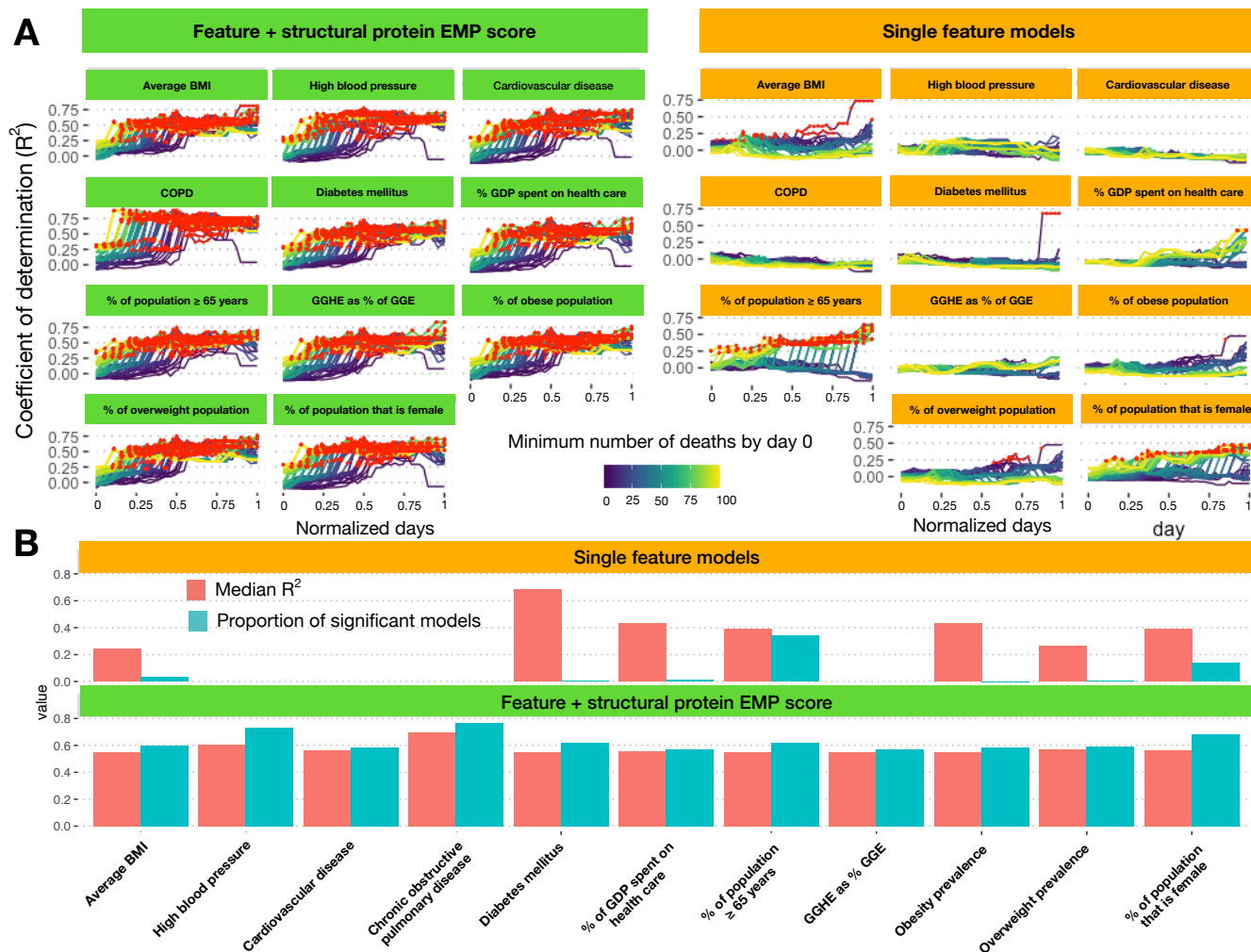


Figure A.21: **Addition of structural protein EMP score significantly improves linear model fit to observed deaths per million.** **A**, Linear models were constructed using either a single risk factor (yellow) or a combination of a risk factor and structural protein EMP scores (green). The x-axis indicates the number of normalized days from when a minimum death threshold was met (line color), and the y-axis indicates the observed adjusted  $R^2$  value. **B**, A summary of results obtained from single feature linear models (top panel, yellow) or the combination models (bottom panel, green). The red bars indicate the median  $R^2$  value achieved by that model and the blue bars indicate the proportion of regressions that were found to be significant ( $F\text{-test} \leq 0.05$ ).

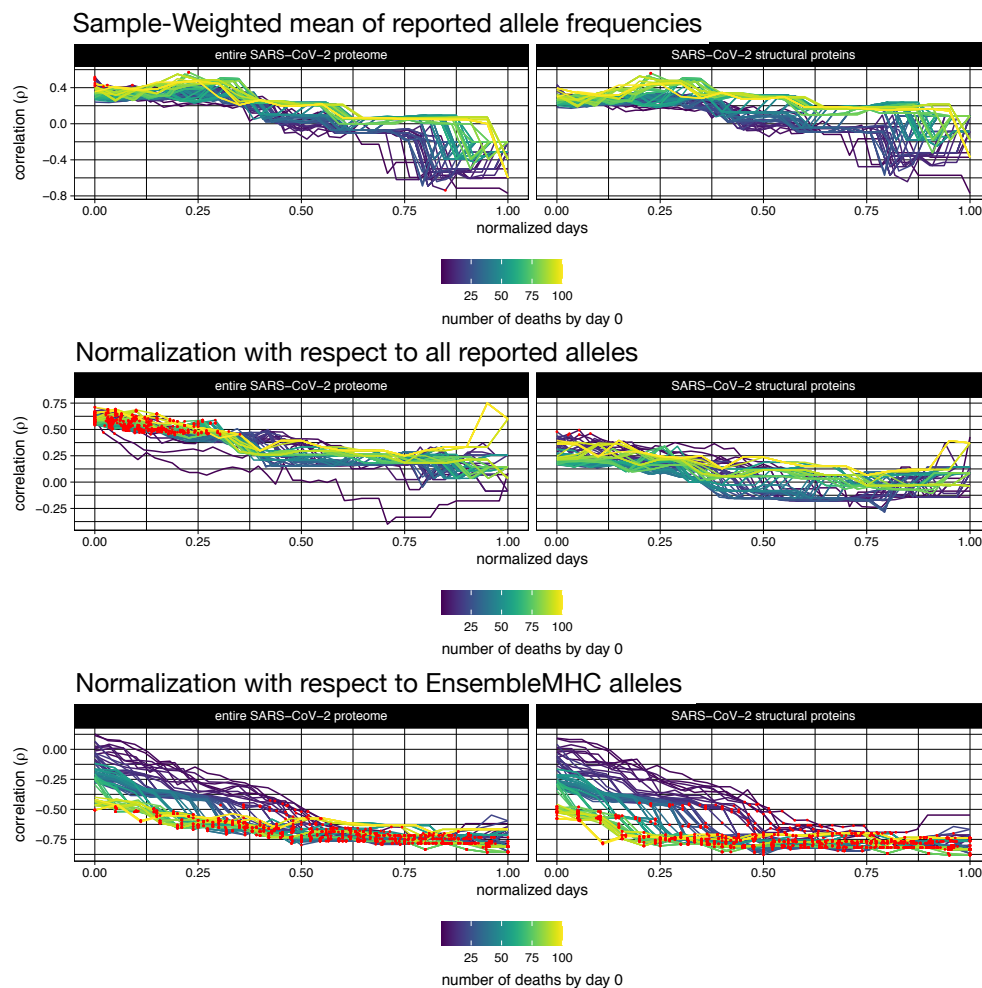


Figure A.22: **EnsembleMHC population score and deaths per million correlation using different allele frequency accounting methods.** The effect of different allele frequency normalization techniques on the reported correlations between SARS-CoV-2 mortality and EMP scores based on the full SARS-CoV-2 proteome (left column) or SARS-CoV-2 structural proteins (right column). **Top panel**, The aggregation of allele frequencies within a particular country by taking the sample-weighted mean of reported frequencies for the 52 selected MHC-I alleles. **Middle panel**, Normalizing allele count with respect to all detected alleles in a given population. **Bottom panel**, Normalizing allele count with respect to only the 52 select alleles.



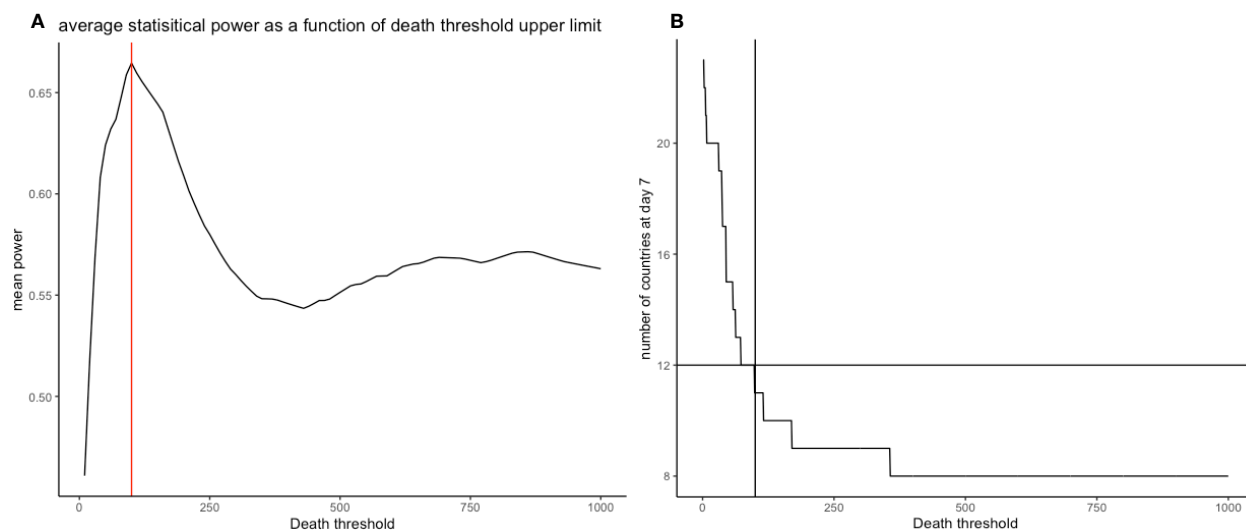


Figure A.23: **Justification of upper limit for death threshold.** **A**, The mean statistical power of all resulting correlations between EnsembleMHC population scores and observed deaths per million at different minimum reported death thresholds. The red line indicates a minimum death threshold of 100 deaths by day 0, the selected upper limit for analysis. **B**, The number of countries remaining at day seven using different minimum death thresholds. The cross bar indicates that there would be more than half of the considered countries remaining at day 7 when using the 100 minimum death threshold.

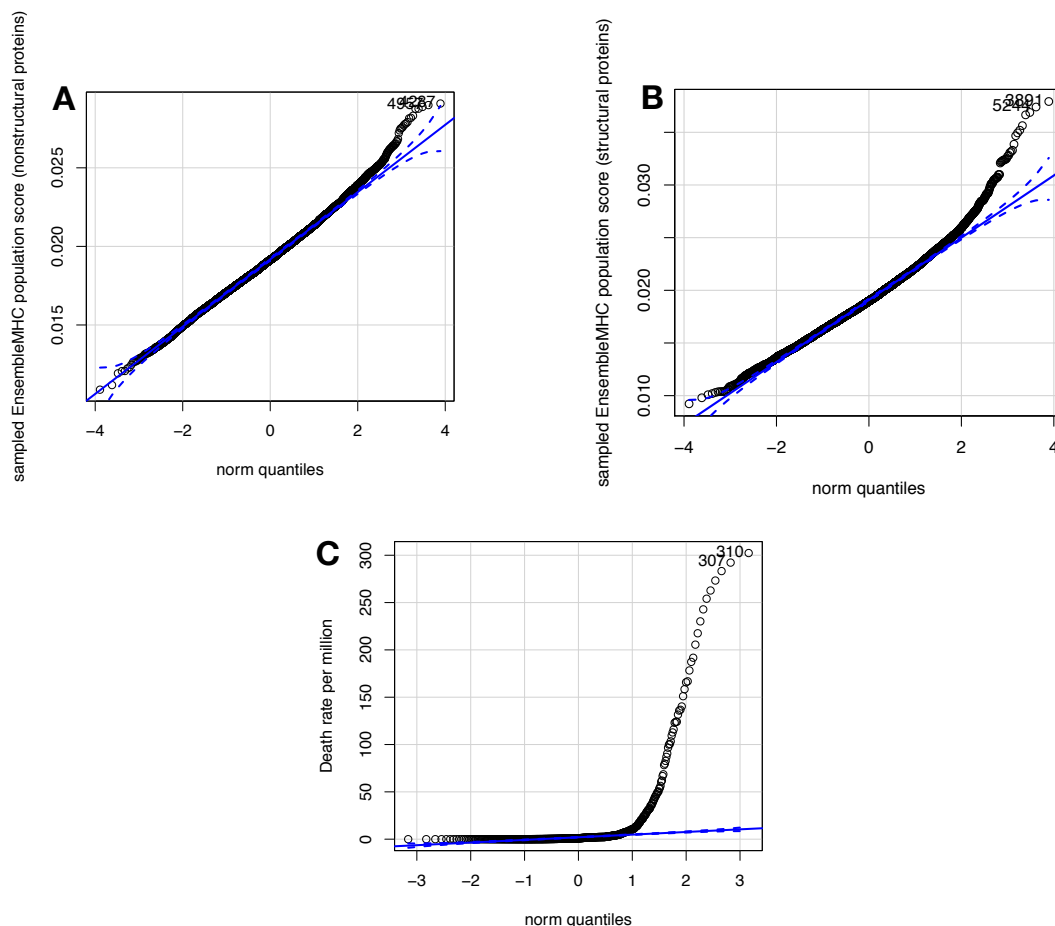


Figure A.24: **Justification of non-parametric correlation analysis.** The use of non-parametric correlation analysis, namely spearman's rho, is justified by the non-normality of the underlying data. EnsembleMHC population scores based on the full SARS-CoV-2 proteome and SARS-CoV-2 structural proteins were calculated for 10,000 simulated countries. Allele frequencies for simulated countries were generated by randomly sampling an observed allele frequency for each of the 52 alleles and re-normalizing to ensure the sum of allele frequencies were equal to one. **A**, The Q-Q plot for the simulated EnsembleMHC population score distribution based on the full SARS-CoV-2 proteome. **B**, The Q-Q plot for the simulated EnsembleMHC population score distribution based on SARS-CoV-2 structural proteins. **C**, The Q-Q plot for all reported deaths per Million. All three quantities show a considerable level of positive skewing, indicating non-normality.

population EnsembleMHC score and death rate correlation

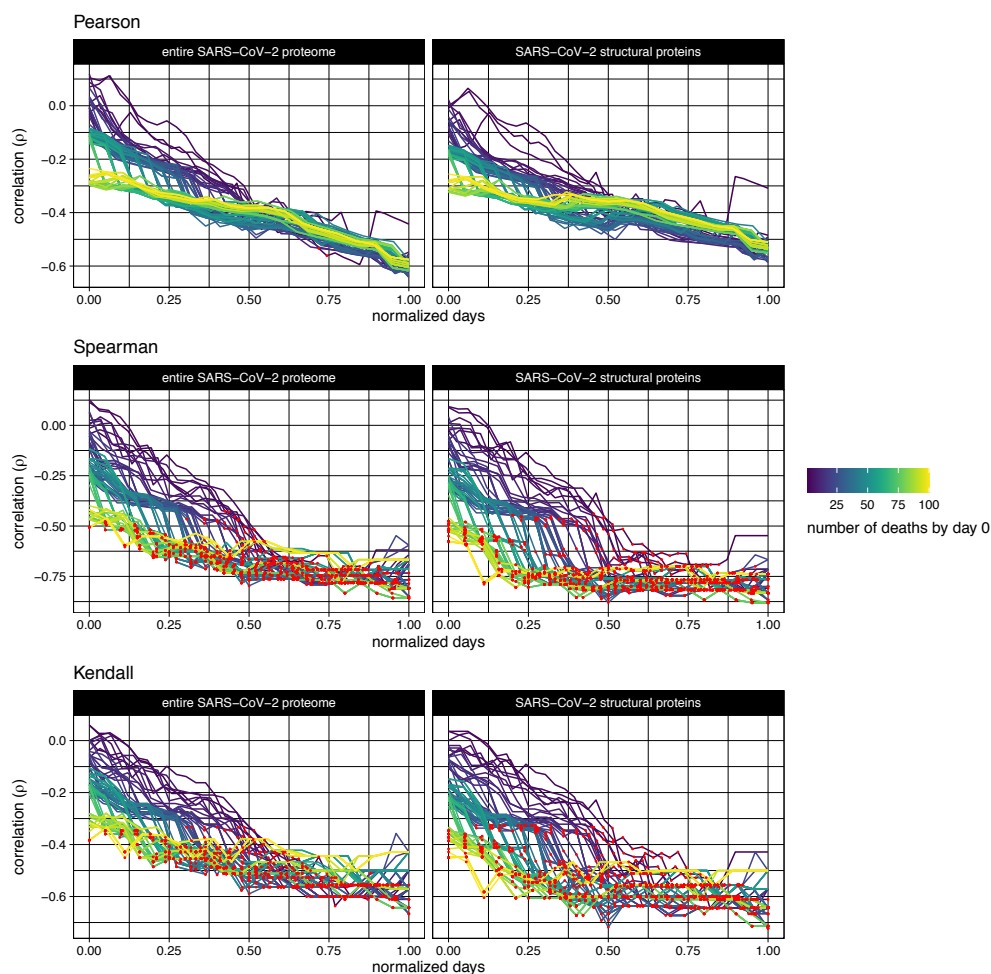


Figure A.25: **The effect of different correlation methods on the relationship between EnsembleMHC score and deaths per million.** The correlation between EnsembleMHC population score with respect to all SARS-CoV-2 proteins (**left column**) or SARS-CoV-2 structural proteins (**right columns**) and deaths per million using Pearson's  $r$  (**top**), Spearman's rho (**middle**), and Kendall's tau (**bottom**). Correlations that were shown to be statistically significant are colored with a red point.

## B tables

Figure B.1: **MHC-I peptide identified by Ensemble MHC**. All identified peptides with a  $peptide^{FDR} \leq 0.05$  (not pictured due to size).

<b>A</b>		<b>B</b>				
<b>Countries</b>		<b>Minimum death threshold</b>	<b>Normalized day: 0.25</b>	<b>Normalized day: 0.5</b>	<b>Normalized day: 0.75</b>	<b>Normalized day: 1</b>
China	5	8	15	23	30	
Japan	10	7	14	20	27	
South Korea	15	7	13	20	26	
Taiwan	20	7	13	20	26	
US	25	7	12	18	24	
Hong Kong	30	7	12	17	23	
France	35	7	12	17	23	
Germany	40	7	12	17	23	
India	45	6	11	17	22	
Italy	50	6	11	17	22	
Russia	55	6	11	17	22	
UK	60	6	11	16	21	
Iran	65	6	11	16	21	
Israel	70	6	11	16	21	
Croatia	75	6	11	16	21	
Romania	80	6	11	15	20	
Netherlands	85	6	11	15	20	
Mexico	90	6	11	15	20	
Ireland	95	5	10	14	19	
Czechia	95	5	10	14	19	
Morocco	100	5	10	14	19	

non-normalized days

Figure B.2: Description of the additional socioeconomic factors selected for analysis. A, The 23 countries for which SARS-CoV-2 population binding capacities were calculated. B, The mapping of normalized days to real days for normalized day quartiles (0.25, , 0.5, 0.75, 1) at select minimum death thresholds.

Figure B.3: **EMP score correlation data.** All correlation data pertaining to the correlations between EMP score and deaths per million. This includes rho estimate, 95% CI, non-normalized days, and sample size for each correlation (not pictured due to size).

<b>A</b>		<b>B</b>		
<b>Countries</b>		<b>Factor</b>	<b>Abbreviation</b>	<b>Description</b>
<b>China</b>		<b>% of population ≥ 65 years</b>	<b>65</b>	Percentage of the population that is 65 years of age or older (2020).
<b>Japan</b>		<b>Average BMI</b>	<b>Avg. BMI</b>	The age-standardized average population body mass index (2016).
<b>South Korea</b>		<b>Cardiovascular disease</b>	<b>CD</b>	The deaths per million due to cardiovascular disease (2016).
<b>US</b>		<b>Chronic obstructive pulmonary disease</b>	<b>COPD</b>	The deaths per million due to complications from chronic obstructive pulmonary disease (2016).
<b>France</b>		<b>Diabetes mellitus</b>	<b>DM</b>	The deaths per million due to complications from diabetes mellitus (2016).
<b>Germany</b>		<b>High blood pressure</b>	<b>BP</b>	The age-standardized percentage of the population with a systolic blood pressure ≥ 140 or diastolic blood pressure ≥ 90 (2015).
<b>India</b>		<b>Obesity prevalence</b>	<b>OBS</b>	The age-standardized percentage of the population with a BMI ≥ 30 (2016).
<b>Italy</b>		<b>Overweight prevalence</b>	<b>OVW</b>	The age-standardized percentage of the population with a BMI ≥ 25 (2016).
<b>Russia</b>		<b>Structural protein EMP score</b>	<b>SP</b>	The SARS-CoV-2 structural protein presentation score.
<b>UK</b>		<b>% of GDP spent on health care</b>	<b>GDP</b>	Current health expenditure (CHE) as percentage of gross domestic product (2017).
<b>Iran</b>		<b>% of total gov. expenditure on health care</b>	<b>GGHE</b>	General government expenditure on health as a percentage of total (2014).
<b>Israel</b>		<b>% of population that is female</b>	<b>SEX</b>	The proportion of the total population that is female (2020).
<b>Croatia</b>				
<b>Romania</b>				
<b>Netherlands</b>				
<b>Mexico</b>				
<b>Ireland</b>				
<b>Czechia</b>				
<b>Morocco</b>				

Figure B.4: **Socioeconomic and health-related risk factors.** **A**, 21 countries were selected for analysis based on the existence of data in the Global Health Observatory data repository and inclusion in the 23 country set used for EMP score analysis. **B**, Descriptions and abbreviations for the selected risk factors. Each factor is labeled with the year that the data was collected. In every case, the most recent data was selected for analysis.